THE TWO-PHOTON DECAY OF METASTABLE ATOMIC

HYDROGEN

D. O'Connell

University of Stirling Institute of Atomic Physics

February, 1975.

ABSTRACT.

The two-photon decay of the $2^2S_{\frac{1}{2}}$ state of atomic hydrogen has been directly observed using a fast coincidence counting technique. A hydrogen metastable beam apparatus has been constructed using a duoplasmatron proton source and charge-exchange in cesium vapour , and its characteristics measured. Tests are described which firmly establish the existance of the two-photon decay of atomic hydrogen, and the observed lifetime due to this process is consistent with the predicted value. The angular distribution of the emitted photons does not · disagree with the predicted $(1 + \cos^2\theta)$ factor.

Acknowledgements.

I want to gratefully acknowledge the support and
stimulation of my principal supervisor, Professor
H. Kleinpoppen, who suggested this project to me.   His
constant encouragement and enthusiasm throughout the
project overcame many obstacles.

I also want to express my appreciation to Dr. A.J. Duncan
who was always willing to discuss difficulties, and able
to solve many of them.

The project could not have been brought to so successful
a conclusion without the assistance of Dr. K.J. Kollath
in the later stages of the work, and his always helpful
advice at all stages.   Thanks are also due to all my
colleagues at Stirling, especially to Dr. D. Hils and
Dr. J. Slevin for many helpful discussions.

I wish to thank the staff of Shared Technical Services
for their active cooperation, and the department technical
staff, who were always willing to offer assistance,
especially Mr. A.J. Duncan.

I acknowledge the financial support of the University
of Stirling.

CONTENTS

I. Introduction.

I.1. Relevant history of the hydrogen atom.

The first real understanding of atomic structure began with Bohr's theory of the hydrogen atom in 1913[1], which at the time satisfactorily explained the gross structure of the spectral lines. Sommerfeld's fine structure theory of 1916, was confirmed in 1926 by Paschen's observations of the fine structure of singly ionized helium and of the Balmer series of hydrogen[2]. After the problems of the intensities were resolved by the introduction of Dirac's theory of the electron and the electron spin, attention was concentrated on the fine structure of the Balmer alpha line. A slight shift in one of the fine structure components seemed to exist, but the resolution of the optical observations was not good enough to show a real discrepancy with the theory. In 1947, the historic experiment of Lamb and Retherford[3] conclusively confirmed the existance of a discrepancy between the Dirac theory and the Balmer alpha fine structure. Using an atomic beam technique and microwave spectroscopy, they found that the $2S_{\frac{1}{2}}$ and the $2P_{\frac{1}{2}}$ levels of atomic hydrogen were not degenerate as predicted by the Dirac theory, but the $2S_{\frac{1}{2}}$ level was shifted upwards in energy by about 4.37×10^{-6} eV, or 1.058 GHz. Bethe[4] immediately interpreted this result in terms of the self-interaction of the electron in non-relativistic, second-order perturbation theory,

obtaining approximately the observed value for what is
now known as the Lamb shift. Since then, the developement
of relativistic quantum electrodynamics by Schwinger,
Tomonaga and Feynman[5] has given an almost complete
picture of the atomic hydrogen energy spectrum.

I.2.   The metastable state.

Before the Lamb shift was discovered, it was realised
that the $2S_{\frac{1}{2}}$ state of atomic hydrogen should be metastable,
in the absence of perturbing effects. The only state
below it in energy was the ground state, on the basis of
the Dirac theory. Electric dipole transitions to the
ground state are strictly forbidden by the parity
selection rule, as are electric quadrupole transitions,
and although magnetic dipole transitions are not strictly
forbidden if the exact Dirac wavefunctions are used, the
lifetime due to this mode of decay was calculated by
Breit and Teller[6] to be about two days.

Maria Goeppert-Mayer in 1931[7] developed the theory of
two-photon decay, through which the parity selection rule,
for transitions between states of the same parity, can be
satisfied by the introduction of virtual transitions to
intermediate states of different parity. In 1940,
Breit and Teller[6] examined the possible modes of decay
of the $2S_{\frac{1}{2}}$ state of atomic hydrogen, and found that in
the absence of perturbing effects, the lifetime was
limited by two-photon decay to the ground state, giving
a transition probability of about 7 s^{-1}. However, they

assumed the degeneracy of the $2S_{\frac{1}{2}}$ and the $2P_{\frac{1}{2}}$ states, and so even very small electric fields would be sufficient to mix them by the Stark effect. Since the $2P_{\frac{1}{2}}$ state was known to have a lifetime of about 1.6×10^{-9} s, it appeared that in practice the $2S_{\frac{1}{2}}$ state would not be metastable in the laboratory.

The discovery of the Lamb shift showed that the lifetime of the $2S_{\frac{1}{2}}$ state was considerably longer in an electric field, (e.g., in a field of 2000 $V.m^{-1}$, the lifetime is of the order of a microsecond), and that metastable beams could be produced and studied in the laboratory.

Because the simultaneous emission of two photons in a single transition gives rise to a form of continuous radiation, the two-photon decay was invoked by Spitzer and Greenstein[7] in 1951 to explain the spectra of certain gaseous planetary nebulae. They calculated the spectrum and transition rate of two-photon emission from the metastable state. Their value for the transition probability is in good agreement with the more accurate calculation of Shapiro and Breit[8] , and the more recent calculation of Klarsfeld[9] of $8.2283 \, Z^6 \, s^{-1}$. They also found that the two-photon decay gives rise to a 'bluish' continuum in the visible region of the spectrum, which appeared consistent with the astronomical observations.

Salpeter[10] and Feinberg[11] pointed out in 1958, that parity and time-reversal violating effects could affect the lifetime of the metastable state. Such an effect could be a permanent electron dipole moment, or as shown

by Zeldovich and Perelemov[12], the presence of neutral
currents in the weak interaction, which would violate
parity.   Evidence for the existance of neutral currents
has recently been reported[13].

The work reported in this thesis is the first observation
of the unperturbed two-photon decay of the metastable
state of atomic hydrogen.

I.3.   The natural decay of metastable states.

This section describes some of the most relevant
observations of the natural decays of metastable
hydrogenlike and heliumlike atoms.   Heliumlike atoms
have two metastable states, the 2^1S_0 and the 2^3S_1 states.
The 2^1S_0 state decays by two-photon emission, and the 2^3S_1
decays predominantly by single photon emission through
the relativistic magnetic dipole process[14].   Although
the 2^3P_2 state of neutral helium decays by an allowed
electric dipole transition, it has been pointed out that
for values of Z greater than about 17, the heliumlike
ions decay predominantly by a single photon magnetic
quadrupole process[15].

The first attempt to observe the spontaneous decay of
a metastable atom was made by Fite et al.[16] in 1959.
They tried to measure the lifetime of the $2S_{\frac{1}{2}}$ state of
atomic hydrogen due to single photon decay, caused by
parity non-conserving effects such as those discussed
in the last section.   They used a thermal beam of
atomic hydrogen excited to the metastable state by

electron impact.   By monitoring the Lyman-alpha signal produced by the metastable atoms in a field-free region, and with a strong electric field applied, they succeeded in setting a lower limit to the single photon decay lifetime of 2.4 10^{-3} s.   This is about 50 times shorter than the predicted two-photon lifetime.

The first direct observation of a two-photon decay was made by Lipeles et al.[18], in 1965.   They observed, in coincidence, the spontaneous two-photon decay of the $2S_{\frac{1}{2}}$ state of singly ionized helium.   An electron bombardment source was used to ionize and excite the atoms which were then accelerated to an energy of about 15 eV.   The ion beam was modulated by rf quenching at the Lamb shift frequency so that the signal originating from the metastables could be seperated from the background.   Since the two-photon spectrum of He^+ is predicted to extend from 30.4 nm to infinity, open-ended photomultiplier tubes were used inside the vacuum system.   A delayed coincidence technique was employed. The beam modulation frequency was 208 Hz and the time spectrum with the quench field on and off were recorded in seperate sections of the multi-channel analyser memory.   Lipeles et al. obtained results consistent with the predicted $(1 + \cos^2 \theta)$ angular distribution, and in a later publication the same group[19] reported a rough spectral distribution, using broad-band filters, not inconsistent with the theoretical predictions.

In 1972, a group from the same laboratory[20] directly measured the natural lifetime of the same state of helium

by a decay-in-flight experiment. A similar ion source
and quenching system was used, connected to an 8-metre
length of pipe fitted with a movable Auger detector.
After corrections were made for collisional quenching,
they measured a lifetime of 2.04 (+0.81,-0.34) ms,
which is consistent with the predicted two-photon
lifetime of 0.1215 Z^{-6} s, or 1.899 ms.

Schmieder and Marrus[21] observed the two-photon decay
of the $2S_{\frac{1}{2}}$ state of hydrogenlike argon in 1970, and
measured its lifetime by a beam-foil time-of-flight method.
They accelerated argon ions (Z = 18) in the +14 charge
state to an energy of 412 MeV in a heavy ion linear
accelerator, and passed them through a thick metal foil
from which they emerged distributed in a variety of
charge states. The fully stripped ions were magnetically
selected and passed through a thin carbon foil in which
the probability of single electron capture was high.
Thus a beam of hydrogenlike argon (Ar^{17+}) was produced.
The two-photon spectrum of this ion extends from 3.34 keV
downwards in energy, so solid-state detectors were used.
A delayed coincidence technique was again used with the
added advantage that the photon energies could be
simultaneously monitored. The sum of the photon energies
that formed the coincidences were found to form a peak at
about 3.3 keV, indicating that the two-photon decay was
indeed being observed. By varying the position of one
of the detectors relative to the foil position, and only
accepting photon energies in the region of 1.67
keV (two-photon peak), the lifetime was measured to be

$(3.54 \pm 0.25)\ 10^{-9}$ s, compared with the predicted value of $3.47\ 10^{-9}$s, taking into account the relativistic magnetic dipole decay rate which increases as Z^{10}, and has a lifetime of $1.1\ 10^{-7}$ s in this case. The mixing of the $2S_{\frac{1}{2}}$ state with the $2P_{\frac{1}{2}}$ state of Ar^{17+} which would result from the parity violating effects as mentioned above, was estimated to be less than $6\ 10^{-4}$ of the $2P_{\frac{1}{2}}$ state.

In subsequent experiments Marrus and Schmieder[14] also observed the forbidden decays of the heliumlike ion Ar^{16+}, the $2^1S_0 \rightarrow 1^1S_0$, the $2^3S_1 \rightarrow 1^1S_0$, and the $2^3P_2 \rightarrow 1^1S_0$ transitions. These results are given in table I.

Table I.

Measured and theoretical lifetimes of Ar^{16+}.

State	t_{expt} (10^{-9} s)	t_{theor} (10^{-9} s)
2^1S_0	2.3 ± 0.3	2.35
2^3S_1	172 ± 30	210
2^3P_2	1.7 ± 0.3	1.49

The 2^1S_0 and the 2^3P_2 lifetimes are in good agreement with theory, but the 2^3S_1 lifetime shows a small discrepancy. However, relativistic corrections to the theory, which have not been taken into account in the above theoretical lifetimes, may improve the agreement . Using the same techniques, the lifetime of hydrogenlike sulphur (S^{15+}) in the $2^2S_{\frac{1}{2}}$ state was found to be, $7.3 \pm 0.7\ 10^{-9}$ s, in agreement with the predicted value of $7.23\ 10^{-9}$ s.

Prior and Shugart[23] in 1971 and Prior[24] in 1972
measured the lifetimes of the 2^1S_0 and the $2^2S_{\frac{1}{2}}$ states
of singly ionized lithium and singly ionized helium,
respectively, using an ion trapping technique. The
ions were generated by electron bombardment and were
contained by electric and magnetic fields, while an
open-ended photomultiplier viewed the storage region.
As the excited ions decayed in the trap, an exponential
decay curve was formed in a multi-channel scaler
coupled to the detector output. In the case of helium,
the ion trap could be irradiated with microwaves at the
Lamb shift frequency, to ensure that it was the $2^2S_{\frac{1}{2}}$ state
under observation. The Li^+ 2^1S_0 state was found to have
a lifetime of $(5.03 \pm 0.26)10^{-4}$ s, in good agreement with
the theoretical value of $5.13\ 10^{-4}$ s. The He^+ $2^2S_{\frac{1}{2}}$
lifetime was measured to be $(1.922 \pm 0.082)\ 10^{-3}$ s,
also in good agreement with the predicted value of,
$1.899\ 10^{-3}$ s. Prior[24] also calculated, on the basis
of the He^+ result, that less than $4.7\ 10^{-5}$ of the $2^2P_{\frac{1}{2}}$
wavefunction was mixed with the $2^2S_{\frac{1}{2}}$, an order of
magnitude improvement over Marrus and Schmieder's
result.

Van Dyck, Johnson and Schugart[25] measured the lifetime
of the 2^1S_0 state of neutral helium in 1971, by direct
observation of the metastable atoms. A beam of helium
atoms was excited to the 2^1S_0 state by the impact of a
short pulse of electrons, after which the atoms drifted
through collimating slits, and through an 80% transparency
copper grid, from which they caused electrons to be

emitted by the Auger effect.   These electrons were collected by an electron multiplier.   After passing through a further drift region of about 5 metres, the beam was collected by a copper plate, from which the Auger electrons were counted by another multiplier. The electron beam was pulsed continuously, and the time distribution of the arrival of the Auger electrons recorded.   By finding the ratio of the number of counts registered by the second detector to that registered by the first, and plotting this ratio on a semi-log scale as a function of the velocity, a straight line was obtained whose slope was the required lifetime.   The result obtained was $(1.97 \pm 1.0)\ 10^{-2}$ s, in agreement with the predicted value of $1.95\ 10^{-2}$s. A similar experiment on the same state of helium was performed by Pearl[26] in 1970, but he obtained a value of $(3.8 \pm 0.8)\ 10^{-2}$ s, in serious disagreement with the value of Van Dyck et al., as well as with theory.

Moos and Woodworth[27] reported in 1973 what must be one of the lowest transition rates ever measured, that for the spontaneous decay of the $2^3S_1 \rightarrow 1^1S_0$ state of neutral helium.   This decay is by a relativistic magnetic dipole process, with a predicted lifetime of 7,874 s.   They observed the 62.556 nm line of this transition in the afterglow of a flowing helium discharge, with a vacuum uv spectrometer.   The metastable density in the discharge tube was determined by measuring the absorption of the 388.9 nm line (2^3S_1 to the 3^3P states) from a helium resonance lamp.

The 2^3S_1 lifetime was thus measured to be 4,150 s, with an experimental uncertainty of a factor of three, which overlaps the predicted value.

Although not a spontaneous transition, the observation of stimulated two-photon emission from the metastable state of atomic hydrogen by Bräunlich and Lambropoulos[28] in 1970, is of direct interest to the present work. These authors used a pulsed Nd-glass laser at a wavelength of 1,590 nm to stimulate the corresponding 137,3 nm photon, as well as a photon of wavelength equal to that of the incident photon. The metastable beam was produced by charge exchange of protons in cesium vapour and the emitted short wavelength photon was observed with a vacuum-uv spectrometer. Anti-Stokes Raman scattering of the laser photons was also observed, in which the incident photon was absorbed, and the emitted photon was at the incident photon frequency, plus the Lyman-alpha frequency. These results were in good agreement with the theory of Zernik[29] on optical quenching of the metastable state.

I.4.   The present experiment.

Although the theory of the two-photon decay is well established, giving good agreement with a number of experiments, it still remained for the decay to be observed and the lifetime to be measured for the simplest atom - hydrogen. The reason for this anomaly lies in the Z^6 dependance of the two-photon decay

probability, which means that hydrogen has the lowest decay rate of all the one-electron atoms.

A number of previous attempts to observe the decay had failed[30,31] without any convincing reason. As a result, it was suspected that the predicted transition probability of $8.228 \, z^6 \, s^{-1}$ might not hold for hydrogen[30]. Although this transition probability has been observed to hold for all the hydrogenlike atoms investigated to the limit of experimental accuracy, it must be admitted that hydrogen is a special case, and so observation of the two-photon decay of hydrogen and a measurement of the corresponding lifetime are of importance and should be investigated.

Previous attempts to observe the hydrogen two-photon decay utilised a hydrogen oven-electron bombardment type of metastable source, similar to the type used in the original Lamb-Retherford experiment. It has been pointed out by Donnally[32] that charge exchange of protons in cesium vapour should give a large cross-section for capture into the metastable state. This has since been verified in a number of experiments[33,34,35]. It was decided to utilise this type of source, with its potentially higher metastable densities in a new attempt to observe the two-photon decay of the $2^2S_{\frac{1}{2}}$ state of atomic hydrogen.

II.   Theory of the decay of the $2S_{\frac{1}{2}}$ state.

The energy diagram of the relevant states of atomic hydrogen is shown in Fig. 1, (neglecting hyperfine structure).   The only states lower in energy than the $2S_{\frac{1}{2}}$ state are the $2P_{\frac{1}{2}}$ and the $1S_{\frac{1}{2}}$ states.   The splitting between the $2S_{\frac{1}{2}}$ and the $2P_{\frac{1}{2}}$ states is known as the Lamb shift.   It will be shown below that of all possible decay modes, the fastest is by the emission of two photons in the electric dipole approximation. Destruction of the metastable state is also discussed.

II.1.   General perturbation theory.

The interaction of electrons and photons can be described by Schroedinger's equation,

$$i\hbar \frac{d}{dt}|\Phi\rangle = H|\Phi\rangle ,$$ II.1.

where $|\Phi\rangle$ is the state vector of the whole system, and H is the Hamiltonian of the whole system, which can be written as,

$$H = H^1 + H^2 + H_i$$ II.2.

$$H_0 = H^1 + H^2$$ II.3.

where H^1 represents the energy of the electrons alone, and H^2 the energy of the photons alone, and H_i their interaction.
If H_i is small compared to H_0, we can treat it as a perturbation on H_0, and so solve the Schroedinger equation independantly for the electrons and the photons.
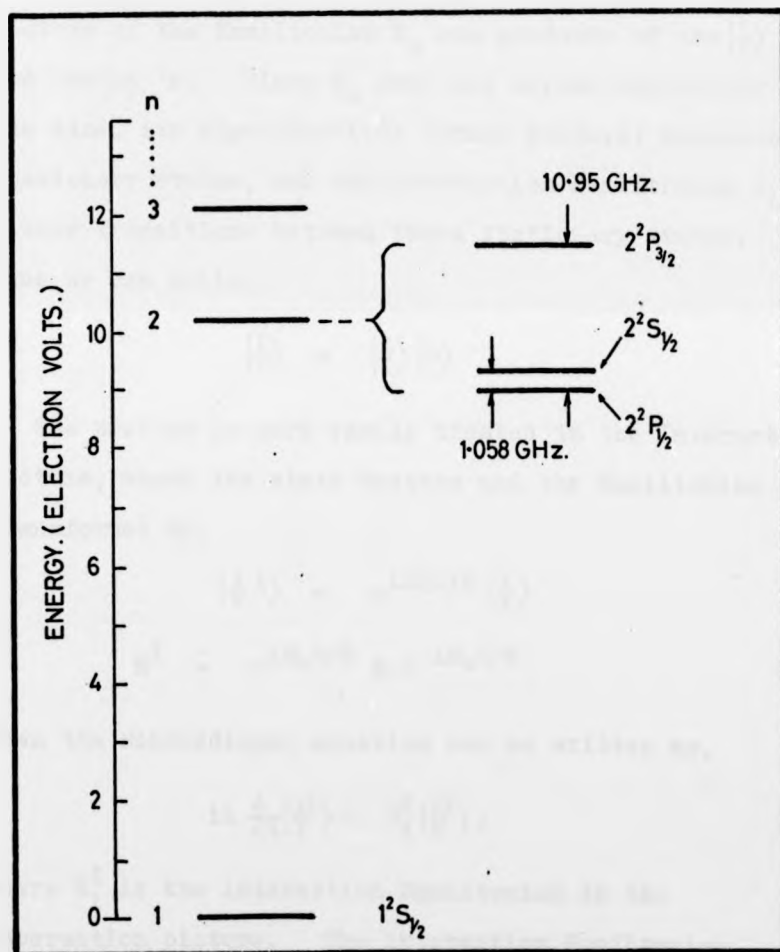
Fig. 1

Energy level diagram of the first two levels of atomic
hydrogen, neglecting hyperfine structure.

$$ih \frac{d}{dt} |\Psi\rangle = H^1 |\Psi\rangle \quad ,$$

$$ih \frac{d}{dt} |n\rangle = H^2 |n\rangle \quad . \qquad \text{II.4.}$$

where $|\Psi\rangle$ is the state vector of the electrons, and $|n\rangle$ is the state vector of the photons. Then the state vectors of the Hamiltonian H_o are products of the $|\Psi\rangle$'s, and the $|n\rangle$'s. Since H_o does not depend explicitly on the time, its eigenfunctions (state vectors) represent stationary states, and the interaction Hamiltonian H_i causes transitions between these stationary states. Thus we can write,

$$|\Phi\rangle = |\Psi\rangle |n\rangle \qquad \text{II.5.}$$

The problem is more easily treated in the Interaction picture, where the state vectors and the Hamiltonian are transformed by,

$$|\Phi^I\rangle = e^{iH_o t/\hbar} |\Phi\rangle \qquad \text{II.6.}$$

$$H^I = e^{iH_o t/\hbar} H e^{-iH_o t/\hbar} \qquad \text{II.7.}$$

Then the Schroedinger equation can be written as,

$$ih \frac{d}{dt} |\Phi^I\rangle = H_i^I |\Phi^I\rangle , \qquad \text{II.8.}$$

where H_i^I is the interaction Hamiltonian in the Interaction picture. The interaction Hamiltonian between the electrons and the photons in the Schroedinger picture is,

$$H_i = -\frac{e}{2m} \vec{A} \cdot \vec{p} + \frac{e^2}{2m} |\vec{A}|^2 \qquad \text{II.9.}$$

A corresponds to the classical vector potential and can be expressed in terms of emission and absorption operators, a^+ and a,[36]

$$A = \sum_{\sigma=1}^{2} \sum_{n} \frac{\hbar}{2\epsilon_{o}\omega V} \hat{e}_{n\sigma}(a_{n}^{+} e^{-i\vec{k}_{n}\cdot\vec{r}} + a_{n} e^{i\vec{k}_{n}\cdot\vec{r}}) \qquad \text{II.10.}$$

where $\hat{e}_{n\sigma}$ is a unit vector in the direction of polarization, and σ determines the two possible polarization states. If P_{f} represents the probability for a transition from an initial state i to a final state f, in the energy range dE_{f}, then the transition probability per unit time is,

$$w = \frac{1}{t} \int_{f} P_{f} \rho_{f} dE_{f} \qquad \text{II.11.}$$

where ρ_{f} is the density of final states.
It can be shown[36] that P_{f} expressed in terms of the scattering operator S, is,

$$P_{f} = \langle \phi_{f} | S | \phi_{i} \rangle^{2} \qquad \text{II.12.}$$

The scattering operator is defined as,

$$S = 1 + \frac{1}{i\hbar} \int_{0}^{t} H_{i}^{I}(\tau) \, d\tau$$

$$+ \left(\frac{1}{i\hbar}\right)^{2} \int_{0}^{t} d\tau_{1} \int_{0}^{\tau_{1}} d\tau_{2} \, H_{i}^{I}(\tau_{1})H_{i}^{I}(\tau_{2})$$

$$\text{II.13.}$$

$$+ \ldots\ldots$$

The first term in the expansion does not give rise to any transitions, since the initial and final states are orthogonal. The second term can give rise to transitions involving both one and two photons. The
The third and subsequent terms give transitions with

two and more photons involved.

II.2.1. Single photon emission.

In this case the transition probability per unit
time is,

$$ w = \frac{1}{t} \int_f \left| \frac{1}{i\hbar} \int_0^t \langle \phi_f | H_i^I | \phi_i \rangle \, d\tau \right|^2 \rho_f dE_f \qquad \text{II.14.}$$

Changing the Hamiltonian to the Schroedinger picture,
and performing the integrations, assuming large t, it
can be shown that,

$$ w = \frac{2\pi}{\hbar} \left| \langle \phi_f | H_i | \phi_i \rangle \right|^2 \rho_f \qquad \text{II.15.}$$

The density of final states for the whole system is,

$$ \rho_f = \frac{2V}{(2\pi)^3} \frac{\omega^2}{\hbar c^3} 4\pi \qquad \text{II.16.}$$

Of the two terms in the interaction Hamiltonian,
equation II.9., only the first term gives to single
photon transitions. The second, being quadratic in
the vector potential, couples the electron to the
radiation field twice, and so gives only two-photon
transitions, and we ignore it here.
Thus using II.16, II.9, and II.10,

$$ w = \frac{e^2 \hbar \omega}{\epsilon_o \pi m^2 c^3} \left| \langle \phi_f | e^{-i\vec{k}\cdot\vec{r}} \, \hat{e}\cdot\vec{\nabla} | \phi_i \rangle \right|^2 \qquad \text{II.17.}$$

The exponential term can be expanded in a Taylor series,

$$ e^{-i\vec{k}\cdot\vec{r}} = 1 - i\vec{k}\cdot\vec{r} + \frac{1}{2}(\vec{k}\cdot\vec{r})^2 - \ldots \qquad \text{II.18.}$$

When II.18 is subtituted into the matrix element II.17
above, the result is analogous to a multipole expansion

in classical radiation theory, the first term being the
electric dipole term, the second the electric quadrupole
and magnetic dipole term, etc.

II.2.2. The electric dipole approximation.

When only the first term in the expansion of the
exponential is included in the matrix element in
equation II.17, the transition probability is given in
what is known as the electric dipole approximation, as,

$$w = \frac{e^2 \hbar \omega}{\epsilon_o m^2 c^3} \left| \langle \Psi_f | \hat{e} \cdot \vec{\nabla} | \Psi_i \rangle \right|^2 \qquad \text{II.19.}$$

Converting the matrix element from the dipole velocity
to the dipole length form,

$$w = \frac{e^2 \omega^3}{\epsilon_o \hbar c^3} \left| \langle \Psi_f | \hat{e} \cdot r | \Psi_i \rangle \right|^2 \qquad \text{II.20.}$$

Applying II.20 to the case of the $2S_{\frac{1}{2}}$ state of atomic
hydrogen, which has only two states of lower energy,
the $2P_{\frac{1}{2}}$ state and the $1S_{\frac{1}{2}}$ ground state, it is easily
seen that the matrix element vanishes between the two
S states by symmetry, an example of the parity selection
rule. The value of the $2S_{\frac{1}{2}}$ to $2P_{\frac{1}{2}}$ matrix element is,
$\sqrt{\sqrt{3}\, a_o^2}$ where a_o is the Bohr radius. Thus the transition
probability for the $2S_{\frac{1}{2}}$ to $2P_{\frac{1}{2}}$ transition is,

$$w(2S \rightarrow 2P) = \frac{e^2 \omega^3}{\pi \hbar \epsilon_o c^3} \sqrt{3}\, a_o^2 = 1.8 \; 10^{-12} \; s^{-1}.$$

which is a negligable rate.

II.2.3. Higher multipole approximations.

In the electric quadrupole approximation, the $2S \rightarrow 1S$
and the $2S \rightarrow 2P$ spontaneous transitions are forbidden by

the " $\Delta l = 0, \pm 2$, except for $l = 0 \rightarrow 0$ " selection rule[37].   In the magnetic dipole approximation, the $2S \rightarrow 2P$ transition is forbidden by the $\Delta l = 0$ selection rule, and the $2S \rightarrow 1S$ transition is forbidden, in the Pauli approximation , since the radial wave functions are orthogonal in this approximation.   However if the exact Dirac wave functions are used, the matrix element of the spin operator is not exactly zero, and so these transitions are not strictly forbidden, but their transition probability is smaller than that for allowed electric dipole transitions by a factor of 10^{-13} for hydrogen.   The lifetime due to this decay mode has been estimated for hydrogen to be about 2 days[6]. In the higher multipole approximations the $2S \rightarrow 1S$ transition is forbidden by the   " No $J = \frac{1}{2} \rightarrow \frac{1}{2}$ " selection rule.

II.3.1. Two photon emission.

We now have to consider both the second and third terms in the expression for the scattering operator, equation II.13.   For the second term, only the second part of the interaction Hamiltonian, equation II.9, contributes to two photon emission.   However, since the wavelength of the radiation being considered, 121.6 nm, is large compared with the dimensions of the region over which the electron wave functions are appreciably different from zero, (a_o), the exponential terms can be taken out of the integral expressions for the matrix elements.   The orthogonality of the electron

wave functions then causes all but the diagonal elements
to vanish.   Thus the $|\vec{A}|^2$ term does not contribute
to two photon emission in this case.

The probability of finding the atom in the final state
f is now,

$$P_f = \left| \langle \phi_f | S' | \phi_i \rangle \right|^2 \qquad \text{II.21.}$$

where from equation II.13,

$$S' = \frac{1}{(i\hbar)^2} \int_0^t d\tau_1 \int_0^{\tau_1} d\tau_2 \, H_i^I(\tau_1) H_i^I(\tau_2) \qquad \text{II.22.}$$

Proceeding as in the single photon case,

$$P_f = 4\left(\frac{e}{m}\right)^4 \sum_j \left| \frac{\langle \phi_f | \vec{p}\cdot\vec{A} | \phi_j \rangle \langle \phi_j | \vec{p}\cdot\vec{A} | \phi_i \rangle}{E_i - E_j} \right|^2 \qquad \text{II.23.}$$

where $\sum_j |\phi_j\rangle\langle\phi_j|$ is the unit operator, and the $|\phi_j\rangle$'s
form a complete set of basis states.

The initial state of the system is,

$$|\phi_i\rangle = |\psi_i\rangle , \quad \text{i.e., no photons,}$$

and the final state is,

$$|\phi_f\rangle = |\psi_f\rangle |\omega_1\rangle |\omega_2\rangle , \quad \text{i.e., two photons.}$$

where ω_1 and ω_2 are the angular frequencies of the photons.
The vector potential now is,

$$\vec{A} = \sqrt{\frac{\hbar}{2\epsilon V}} \left[\frac{\hat{e}_1}{\sqrt{\omega_1}} a_1^+ e^{-i\vec{k}\cdot\vec{r}} + \frac{\hat{e}_2}{\sqrt{\omega_2}} a_2^+ e^{-i\vec{k}\cdot\vec{r}} \right] \qquad \text{II.24.}$$

Substituting equation II.23 in equation II.23,

$$P_f = \frac{e^4\hbar^2}{m^4\epsilon_\circ^2 V^2} \frac{1}{\omega_1\omega_2} \left| \sum_j \frac{\langle \psi_f | \hat{e}_1 \cdot \vec{p} | \psi_j \rangle \langle \psi_j | \hat{e}_2 \cdot \vec{p} | \psi_i \rangle}{E_i - E_j'} \right.$$

$$\left. + \frac{\langle \psi_f | \hat{e}_2 \cdot \vec{p} | \psi_j \rangle \langle \psi_j | \hat{e}_1 \cdot \vec{p} | \psi_i \rangle}{E_i - E_j''} \right|^2 \qquad \text{II.25.}$$

The two terms can be illustrated by Feynman diagrams, as shown in Fig. 2,
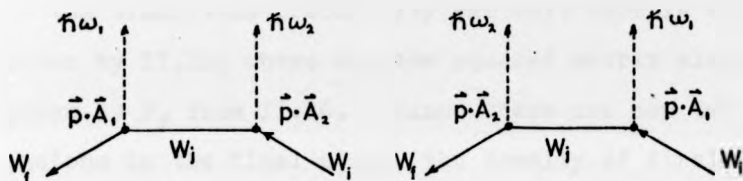
Fig. 2.

The W's are the electron energies, the solid lines represent the electron, the dashed lines the photons, and the vertices, the interactions.   The decay can proceed by either diagram, so the probabilities are summed.

We have,

$$E_i = W_i, \qquad E_j' = W_j + \hbar\omega_1,$$

$$E_j'' = W_j + \hbar\omega_2, \quad E_f = W_f + \hbar\omega_1 + \hbar\omega_2.$$

So,

$$(E_i - E_j') = W_i - W_j - \hbar\omega_1 = \hbar(\omega_{ij} - \omega_1),$$

$$(E_i - E_j'') = W_i - W_j - \hbar\omega_2 = \hbar(\omega_{ij} - \omega_2).$$

Where $\hbar\omega_{ij}$ is the energy difference between states W_i and W_j.

Using these equations, and changing from the dipole velocity to the dipole length form of the matrix element, II.25 becomes,

$$P_f = \frac{e^4}{\epsilon_\circ^2 V^2} \omega_1 \omega_2 \left| \sum_j \frac{\langle \Psi_f | \hat{e}_1 \cdot \vec{r} | \Psi_j \rangle \langle \Psi_j | \hat{e}_2 \cdot \vec{r} | \Psi_i \rangle}{\omega_{ij} - \omega_1} \right.$$

$$\left. + \frac{\langle \Psi_f | \hat{e}_2 \cdot \vec{r} | \Psi_j \rangle \langle \Psi_j | \hat{e}_1 \vec{r} | \Psi_i \rangle}{\omega_{ij} - \omega_2} \right|^2$$

II.26.

. The transition probability per unit time is again given by II.15, where now the squared matrix element is given by P_f from II.26. Since there are now two photons in the final state, the density of final states can be seen to be,

$$\rho_f = \rho_1 \rho_2 \cdot \hbar d\omega_1 \qquad \text{II.27.}$$

Thus,

$$w = \frac{2e^4}{\epsilon_\circ^2 \hbar^2 c^6 \pi^3} \langle |M|^2 \rangle_w \omega_1^3 \omega_2^3 \, d\omega_1 \qquad \text{II.28.}$$

$$= A(\omega_1) \, d\omega_1$$

where M is the matrix element in II.26, and the average is taken over the directions of propagations of the photons, (through the density of final states function). The total transition probability, A is obtained by integrating II.28,

$$A = \tfrac{1}{2} \int_0^{\omega_{if}} A(\omega_1) \, d\omega_1 \qquad \text{II.29.}$$

where $\hbar\omega_{if}$ is the energy difference between the initial and final states. The factor of $\tfrac{1}{2}$ is introduced to

avoid counting each pair of photons twice.   By
conservation of energy, we must have,

$$\omega_1 + \omega_2 = \frac{E_i - E_f}{\hbar} = \omega_{if} \qquad \text{II.30.}$$

The intermediate states $\left| \Psi_j \right\rangle$ in equation II.28, are
P states, since the virtual transitions involved are
electric dipole transitions.   These virtual transitions,
which need not conserve energy, can occur to all
possible intermediate states, continuum as well as
discrete, so the summation in the matrix element must
also be considered as an integral over the continuum.

II.3.2.   Angular distribution.

The dipole length operator $\vec{r}$ in equation II.26, is
diagonal in nuclear and electronic spin, so the effects
of fine and hyperfine structure can be neglected in
applying equation II.28.   Then the S levels can be
considered single and the P levels triply degenerate,
(m = +1, 0, -1).   Following Breit and Teller[6], we
can consider each P level in terms of three linearly
independent P-state wave functions, having the
transformation properties of the cartesian coordinates,
x, y, and z, and denoted by, α , β , and γ .

For each state j, we have,

$$\sum_{\alpha, \beta, \gamma.} (\hat{e}_1 \cdot \vec{r})_{fj} (\hat{e}_2 \cdot \vec{r})_{ji} = (e_{1x}x)_{f\alpha}(e_{2x}x)_{\alpha i}$$
$$+ (e_{1y}y)_{f\beta}(e_{2y}y)_{\beta i}$$
$$+ (c_{1z}z)_{f\gamma}(e_{2z}z)_{\gamma i}$$

Or,

$$\sum_{\alpha,\beta,\gamma} (\hat{e}_1\cdot\vec{r})_{fj}(\hat{e}_2\cdot\vec{r})_{ji} =$$

$$z_f z_f(e_{1x}e_{2x} + e_{1y}e_{2y} + e_{1z}e_{2z}) \qquad II.31.$$

using the symmetry and orthonormality of the wave functions, and where the matrix elements $\langle\Psi_f|A|\Psi_j\rangle$ are denoted by $(A)_{fj}$.

The sum over j is then,

$$\hat{e}_1\cdot\hat{e}_2 \sum_{n=1}^{\infty}\left[\frac{1}{\omega_{in}-\omega_1} + \frac{1}{\omega_{in}-\omega_2}\right] z_{fn}z_{ni} \qquad II.32.$$

where n is the principal quantum number of the P states, and the matrix elements z_{fn} are between the state f and the state of type γ with principal quantum number n.

The above analysis shows that the transition probability has a dependence on the polarizations of the photons of the form $(\hat{e}_1\cdot\hat{e}_2)^2$. When the photon detectors used are not polarization sensitive, as in the present experiment, the transition probability must be averaged over the directions of polarization.

We chose two coordinate systems, x, y, z, and x', y', z', with unit vectors along the axes, $\hat{x},\hat{y},\hat{z}$, and $\hat{x}'$, $\hat{y}'$, $\hat{z}'$, respectively, so that the propagation vector $\vec{k}_1$ of photon 1 points along $\hat{z}$, and propagation vector $\vec{k}_2$ of photon 2 points along $\hat{z}'$. and $\hat{x} = \hat{x}'$. Then the polarization vectors are,

$$\hat{e}_1 = \cos\phi\,\hat{x} + \sin\phi\,\hat{y}$$

$$\hat{e}_2 = \cos\phi'\hat{x}' + \sin\phi'\hat{y}'$$

where φ is the angle between $\hat{e}_1$ and the x axis, and φ' is the angle between $\hat{e}_2$ and the x' axis.   Then,

$$\hat{e}_1 \cdot \hat{e}_2 = \cos\varphi \cos\varphi' + \sin\varphi \sin\varphi' \cos\theta, \qquad \text{II.33.}$$

where θ is the angle between the propagation directions of the photons, i.e., $\cos\theta = \hat{y} \cdot \hat{y}' = \hat{z} \cdot \hat{z}'$.
Squaring II.33 and averaging over φ and φ' independently, we obtain,

$$\langle(\hat{e}_1 \cdot \hat{e}_2)^2\rangle_{av} = \tfrac{1}{4}(1 + \cos^2\theta) \qquad \text{II.34.}$$

Therefore if the polarizations are averaged, the photon pair have maximum probability of being emitted with the angle between their directions of propagation being either 0° or 180°.

If the average is taken over the propagation directions as well as over the polarizations, then it is easily seen that,

$$\langle(\hat{e}_1 \cdot \hat{e}_2)^2\rangle_{av} = \tfrac{1}{3} \qquad \text{II.35.}$$

II.3.3.   Spectral distribution.

From the energy conservation condition, equation II.30, it can be seen that the transition probability as given by equation II.28, has a single maximum at, $\omega_1 = \omega_2 = \tfrac{1}{2}\omega_{if}$, where ω_{if} is the Lyman-alpha frequency, and is symmetrical about ω_{if}.   Fig. 3 shows $A(\omega_1)$ plotted from values tabulated by Spitzer and Greenstein[17].

The transition probability per unit time as a

A(ω) (arb. units)
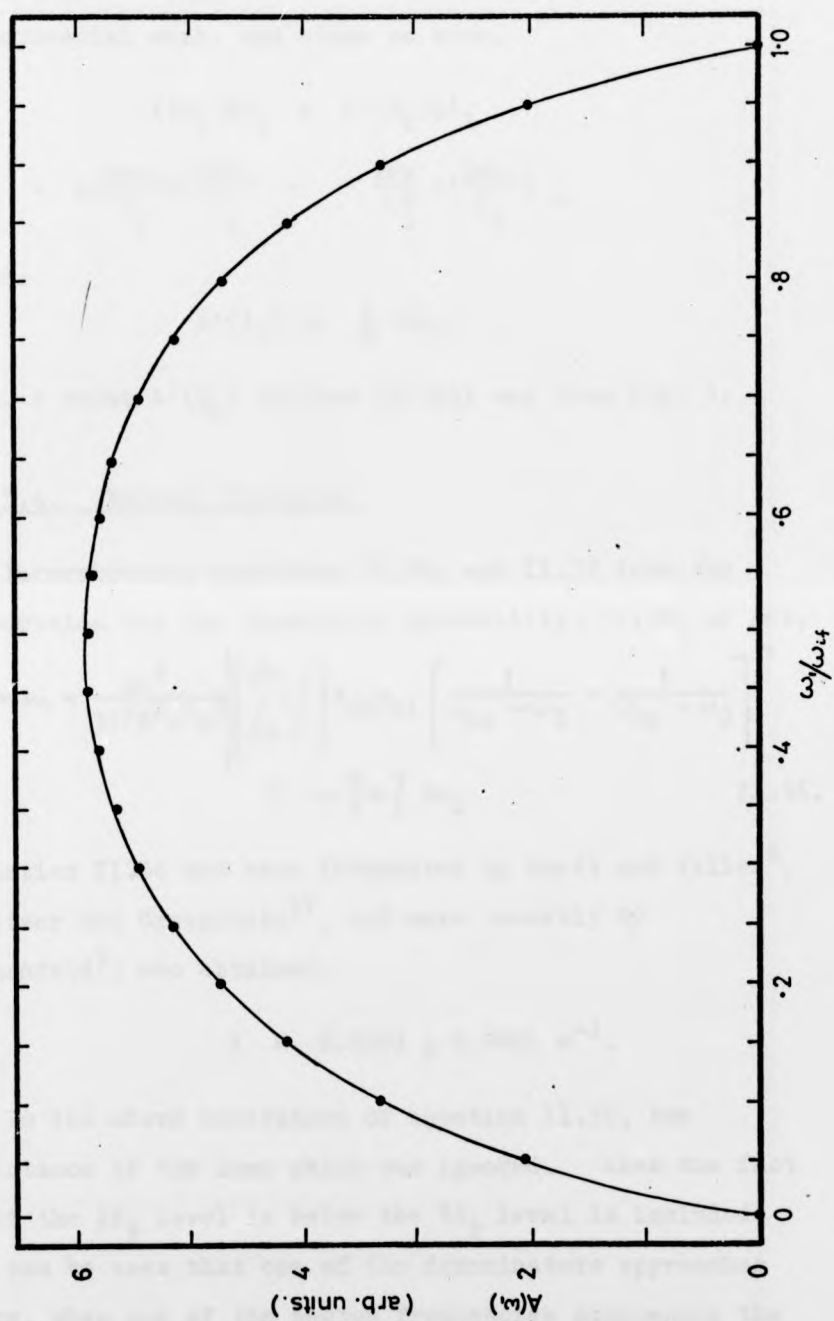
ω/ω_{04}

Fig. 3.

Predicted two-photon spectrum plotted on an energy scale.

function of wavelength is of much more interest in experimental work, and since we have,

$$A(\omega_1)d\omega_1 = A'(\lambda_1)d\lambda_1$$

$$= A(\frac{2\pi c}{\lambda_1})d(\frac{2\pi c}{\lambda_1}) = -\frac{2\pi c}{\lambda_1^2}A(\frac{2\pi c}{\lambda_1})d_1$$

then,

$$A'(\lambda_1) \propto \frac{1}{\lambda^2}A(\omega_1) \quad .$$

Fig. 4 shows $A'(\lambda_1)$ derived in this way from Fig. 3.

II.3.4. Natural lifetime.

Incorporating equations II.35, and II.32 into the expression for the transition probability, II.28, we get,

$$A(\omega_1)d\omega_1 = \frac{2e^4}{3\epsilon_o^2\hbar^2c^6\pi^3}\left|\left[\sum_{n=2}^{\infty}+\int\right]z_{fn}z_{ni}\left[\frac{1}{\omega_{2n}-\omega_1}+\frac{1}{\omega_{2n}-\omega_2}\right]\right|^2$$
$$\times \omega_1^3\omega_1^3 \, d\omega_1 \qquad \qquad \text{II.36.}$$

Equation II.36 has been integrated by Breit and Teller[6], Spitzer and Greenstein[17], and more recently by Klarsfeld[9], who obtained,

$$A = 8.2283 \pm 0.0001 \, s^{-1}.$$

In the above derivation of equation II.36, the existence of the Lamb shift was ignored. When the fact that the $2P_{\frac{1}{2}}$ level is below the $2S_{\frac{1}{2}}$ level is included, it can be seen that one of the denominators approaches zero, when one of the photon frequencies approaches the Lamb shift frequency, and consequently an infinitely large value is obtained for the transition probability.
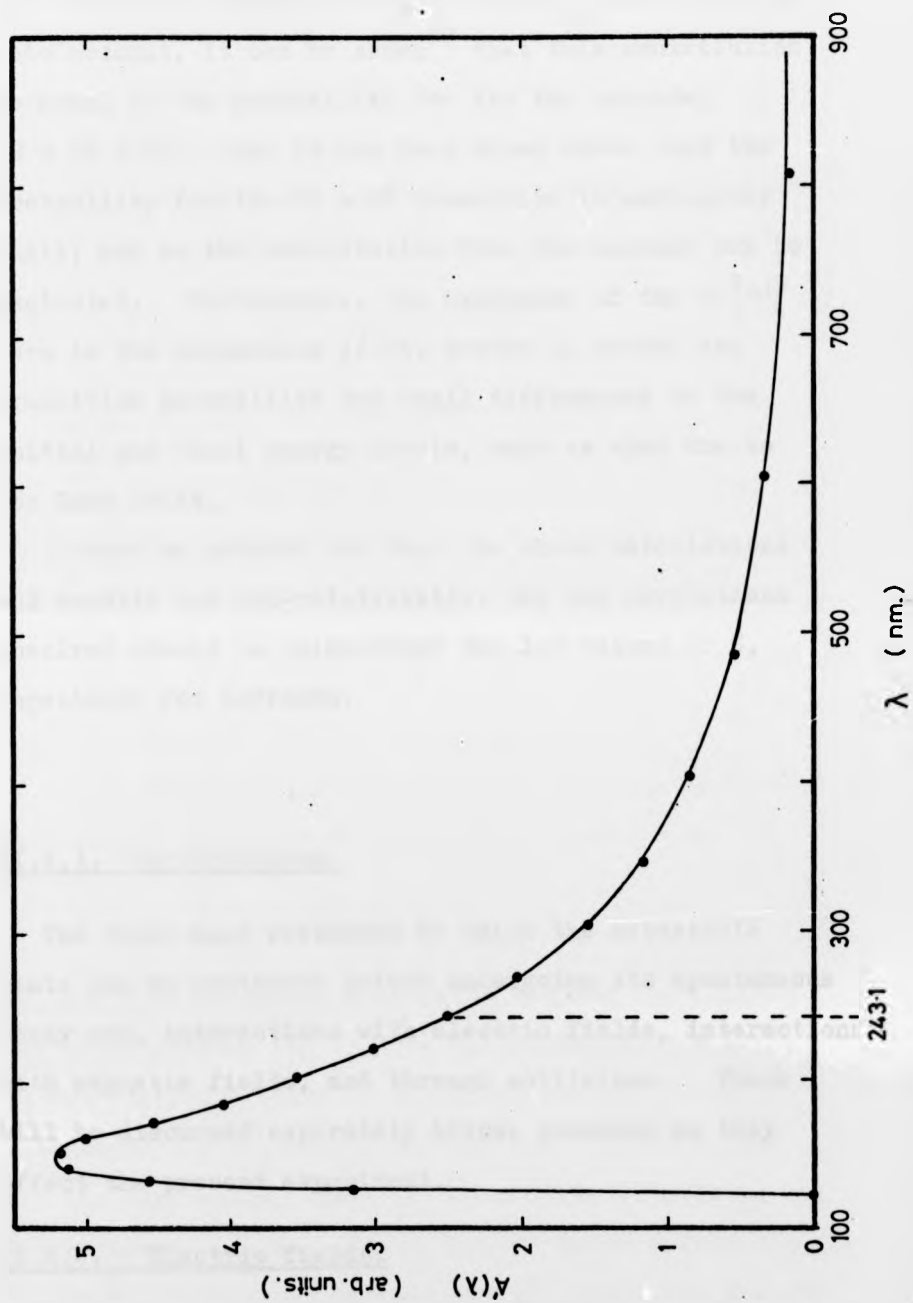
Fig. 4.

Predicted two-photon spectrum plotted on a wavelength scale.

But when the radiation width of the $2P_{\frac{1}{2}}$ state is taken
into account, it can be shown[38] that this contribution
is equal to the probability for for the cascade,
$2S \to 2P \to 1S$.   But it has been shown above that the
probability for the $2S \to 2P$ transition is negligibly
small, and so the contribution from the cascade can be
neglected.   Furthermore, the existance of the $\omega_1^3 \omega_2^3$
term in the expression II.36, serves to reduce the
transition probability for small differences of the
initial and final energy levels, such as that due to
the Lamb shift.

It must be pointed out that the above calculations
and results are non-relativistic, but the corrections
involved should be unimportant for low values of Z,
especially for hydrogen.

II.4.1. Perturbations.

The three main processes by which the metastable
state can be destroyed before undergoing its spontaneous
decay are, interactions with electric fields, interactions
with magnetic fields, and through collisions.   These
will be discussed seperately below, inasmuch as they
affect the present experiment.

II.4.2. Electric fields.

If an electric field is applied to a hydrogen atom in
the metastable state, its lifetime is reduced due to

Stark mixing of the 2P states with the metastable $2S_{\frac{1}{2}}$
state.   It is to be expected that the $2P_{\frac{3}{2}}$ state gives
a much smaller contribution to electric field quenching
than the $2P_{\frac{1}{2}}$ state, since it is much further from the
S state.   Neglecting the $2P_{\frac{3}{2}}$ state, Bethe and Salpeter[37]
obtain for the metastable lifetime in an electric field E,

$$t_s = t_p \left[1 + \frac{\alpha^2}{(1 - \sqrt{1 + \alpha^2})^2} \right] \qquad \text{II.37.}$$

with, $\alpha = \dfrac{2\ 3\ ea_o E}{L}$,

where t_p is the lifetime of the $2P_{\frac{1}{2}}$ state, E is the
electric field strength, and L is the Lamb shift.   For
low field strengths, (i.e., $\alpha \ll 1$, or $E \lesssim 100V\ cm^{-1}$),

$$t_s = t_p \left[\frac{475}{E} \right]^2 \qquad \text{II.38.}$$

with E expressed in Volts per centimetre.

Using time-dependent perturbation theory, Lamb and
Retherford[3] developed a more general expression,

$$\frac{1}{t_s} = \frac{|\langle b | e\vec{E}\cdot\vec{r} | a \rangle|^2}{\hbar^2(\omega^2 + \gamma^2/4)} \cdot \gamma \qquad \text{II.39.}$$

where $\hbar\omega$ is the energy difference between the initial
and final states, $|a\rangle$ and $|b\rangle$ respectively, $\gamma = 1/t_p$
is the radiation width of the final state.   When $|a\rangle$
represents the $2S_{\frac{1}{2}}$ state, and $|b\rangle$ the $2P_{\frac{1}{2}}$ state, and
$\hbar\omega$ the Lamb shift, the expression II.39 reduces to the
Bethe formula II.37.   Since, as can be seen from Fig. 1,
the energy difference between the $2S_{\frac{1}{2}}$ state and the $2P_{\frac{3}{2}}$
state is about 10 times the energy difference between
the $2S_{\frac{1}{2}}$ state and the $2P_{\frac{1}{2}}$ state, it follows that the

contribution of the $2P_{\frac{3}{2}}$ term is about 1% of that of
the $2P_{\frac{1}{2}}$ term, justifying its neglect in the Bethe
formula II.37.   Drake[39] interpreted the quenching of
a metastable atom on suddenly entering an electric
field in terms of a two-photon induced transition, with
one of the photons at zero frequency, to deduce the
polarization of the emitted Lyman-alpha radiation.   (The
$2P_{\frac{3}{2}}$ state must be included here to obtain the correct
polarization value.)

II.4.3.   Magnetic fields.

Under the influence of an external magnetic field,
the 2S and 2P levels split into a number of components
corresponding to the possible values of the magnetic
quantum number m_j,   i.e., two for the $j = \frac{1}{2}$ state and
four for the $j = \frac{3}{2}$ state.   Because of the separation
of the $2S_{\frac{1}{2}}$ and the $2P_{\frac{3}{2}}$ states, we can again neglect the
latter.   At about 575 gauss there is a crossing between
the $2S_{\frac{1}{2}}$ ($m_j = -\frac{1}{2}$) and the $2P_{\frac{1}{2}}$ ($m_j = +\frac{1}{2}$) levels.   Fields
of this magnitude can easily be excluded from an
apparatus, but lower fields can still quench the
metastable state through the motional electric field $\vec{E}$,
for atoms moving in a magnetic field $\vec{B}$, with velocity $\vec{v}$,

$$\vec{E} = \vec{v} \times \vec{B} \hspace{3cm} \text{II.40.}$$

producing Stark mixing.

II.4.4. Collisions.

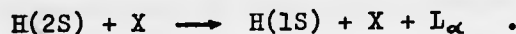The quenching of metastable hydrogen atoms through collisions can occur via three main processes,

(1) electron loss,

$$H(2S) + X \longrightarrow H^+ + X + e^- \quad ;$$

(2) electron capture,

$$H(2S) + X \longrightarrow H^- + X^+ \quad ;$$

(3) de-excitation,

$$H(2S) + X \longrightarrow H(1S) + X + L_\alpha \quad .$$

At thermal energies, the de-excitation process is the only possible reaction, due to the low energy available. Fite et al.[16] found that water vapour had a cross-section for quenching metastables as large as $1000 \ \pi a_0^2$, while molecular hydrogen and nitrogen gave about $100 \ \pi a_0^2$. The high value for water vapour can be understood in terms of the long-range permanent dipolar field of the molecule, while the other molecules have only quadrupolar fields. As the energy of the projectiles is increased, the de-excitation process becomes less important due to the shorter time spent in the target field.

Electron capture cross-sections are also found to decrease with increasing energy[40], but more slowly than the de-excitation process. Electron loss cross-sections have been observed to increase with increasing energy,[40a] and are relatively unimportant at the moderate energies of interest here, (about 1 keV, or 0.2 a.u.).

The only target species we need consider are the main constituents of the background gas, which were observed

to be, (using a quadrupole mass spectrometer), water vapour, molecular hydrogen and molecular nitrogen. The total quenching cross-section for H_2O and N_2 have been measured by Dose et al.[41] in the energy range of 2 → 60 keV. Their results at 2 keV give about $25 \pi a_o^2$ for both species, increasing with decreasing energy. Extrapolated to 1 keV, the probable upper limit is about $40 \pi a_o^2$. Byron et al.[42] have measured the total quenching cross-section for molecular hydrogen and nitrogen in the energy range of interest, and found a value of about $8\pi a_o^2$ for both, at an energy of 1 keV. Although the two results are not consistent, we can take about $40 \pi a_o^2$ as an upper limit for quenching of the metastables by the background gas in the region of 1 keV.

The effects of the perturbations are two-fold; (1), they reduce the metastable density, and (2), if they occur within the observation region, can give rise to a radiation background.

Electric and magnetic fields only contribute to (1), since these processes give rise to Lyman-alpha photons, which the photomultipliers are not sensitive to. Since the time taken for the metastable atoms, at 1 keV energy, to traverse the apparatus is about $2 \ 10^{-6}$ s, perturbations must be kept low enough so that the reduced lifetime is, say, at least 10 times this value. This requirement gives, from equation II.38, that the average electric field E along the beam length must be,

$$E \lesssim 4.5 \text{ V cm}^{-1} \quad ,$$

and the magnetic field, perpindicular to the beam axis, must be,

$$B \lesssim 10^{-3} \text{ Tesla, or 10 gauss.}$$

Collisions with the background gas can give rise to processes (1) and (2). If we take the average background pressure in the metastable beam path as about 10^{-7} torr, or a thickness over 1 metre of, $\pi = 3.5 \ 10^{15}$ molecules m^{-2}, then the fractional loss of metastables over this length can be approximated as,

$$f \cong \pi.\sigma$$

where σ is the cross-section for metastable destruction, about 40 πa_0^2 or $4 \ 10^{-19} \ m^{-2}$, from above. This gives,

$$f \cong 1.4 \ 10^{-3}$$

a negligible loss.

For process (2), we can assume, as a worst case, that each collision gives rise to a detectable photon, through excitation of the background gas, then the radiation background produced by collisional quenching can be approximated as,

$$R \cong j(2S)\pi.\sigma$$

where $j(2S)$ is the metastable flux, in atoms per second, and π is now the thickness of the background gas in the observation region. For a pressure of 10^{-8} torr, and an observation region length of about $3 \ 10^{-2} \ m$, $\pi = 10^{13} \ m^{-2}$. We then have,

$$R \cong 2.5 \ 10^4 \ s^{-1}$$

the significance of which will be discussed in section III.13.

III.   Apparatus.

III.1.   Introduction.

A schematic diagram of the main components of the
apparatus is shown in Fig. 5.   A duoplasmatron ion
source, (1), with electrostatic lens system, (2), and
analysing magnet, (3), are used to produce a proton beam.
The protons are converted into hydrogen atoms in a
cesium charge-exchange cell, (7).   The detection region
consists of an ultra-violet transmitting quartz tube, (11),
which is observed by a pair of photomultiplier tubes, (10).

After leaving the detection region, the beam is
monitored by a photomultiplier, (14), which detects the
Lyman-alpha radiation emitted by the metastable atoms
on entering the quench field, (13), and by a neutral
detector/faraday cup, (15), which measures the current
of the protons or of the neutrals in the beam, using a
reversible potential on the guard ring.

The fast photomultiplier tubes are connected to a
delayed coincidence circuit, which monitors the
distribution of arrival time differences of pulses from
the photomultiplier anodes.   This method is described
by Bell[43].   After leaving the charge-exchange cell,
but before entering the detection region, the beam
passes through two pre-quenching systems, (8), and (9).
The pre-quench plates, (8), fulfils two functions, the
removal of the charged fraction from the beam, and the
periodic pre-quenching of the metastables, in order that

the background can be monitored.   The pre-quench
wires, (9), are used to fully quench the metastables to
provide a zero check.

III.2.   Production of the metastable beam.

The traditional source of metastable hydrogen atoms
has until recently been of the Lamb-Retherford type,
consisting of an oven to dissociate molecular hydrogen,
and an electron beam to excite the atoms to the
metastable state.   With a source of this type, the beam
intensity and collimation obtainable have been limited
by the cross-section for the excitation, $0.16 \ \pi a_o^2$ [44],
the electron beam intensity obtainable and the large
gas loads that must be handled by the vacuum system.

Another method which has been used to form a
metastable beam is by charge transfer of protons in a
gas target.   The maximum cross-sections for this process
are small, however and occur at relatively high energies,
for example, for molecular hydrogen, about $0.27 \ \pi a_o^2$,
at 30 keV, and for argon, about $0.28 \ \pi a_o^2$ at the same
energy.[45].

In 1964, Donnally et al.[32] proposed an improved
source of low-energy metastable hydrogen atoms using
the nearly resonant process of charge-exchange of
protons in cesium vapour,

$$H^+ \ + \ Cs \ \longrightarrow \ \left(H(2S), \ H(2P)\right) + Cs^+ - 0.49 \ eV. \qquad III.1.$$
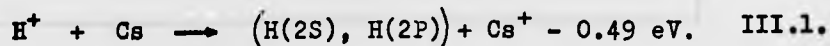
Massey[47] has pointed out that when the energy defect

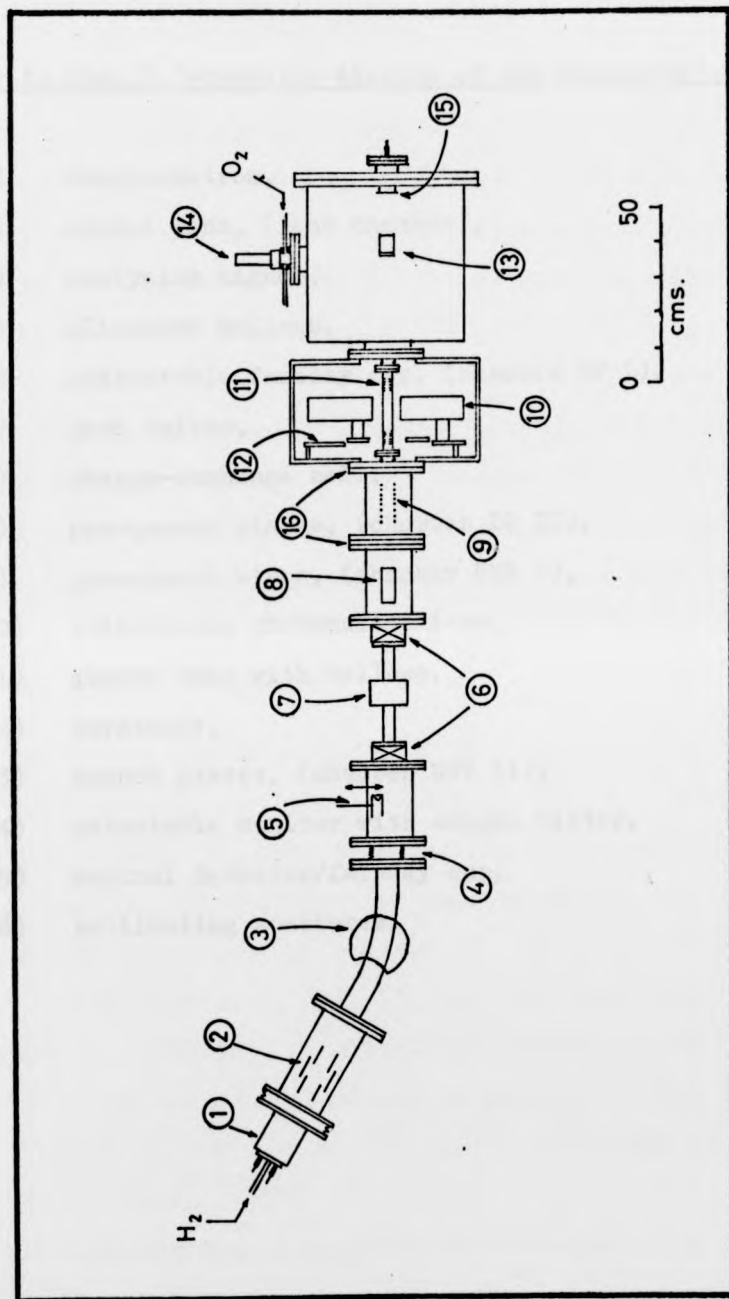**Fig. 5.**

Schematic diagram of the apparatus. (For key, see page 36.)

Key to Fig. 5,'schematic diagram of the apparatus'.

(1)   duoplasmatron,

(2)   einzel lens, (lens chamber),

(3)   analysing magnet,

(4)   alignment bellows,

(5)   retractable faraday cup, (chamber DP I),

(6)   gate valves,

(7)   charge-exchange cell,

(8)   pre-quench plates, (chamber DP II),

(9)   pre-quench wires, (chamber UHV I),

(10) coincidence photomultipliers,

(11) quartz tube with bellows,

(12) turntable,

(13) quench plates, (chamber UHV II),

(14) metastable monitor with oxygen filter,

(15) neutral detector/faraday cup,

(16) collimating apertures.

for the charge changing process is small, the cross-section is expected to be large and occur at low energies.   This has since been verified in a number of experiments.   Pradel et al.[35] have found that the maximum cross-section for the above process is about $60\ \pi a_o^{\ 2}$, at an energy of about 600 eV, and at a cesium target thickness of about $1.2\ 10^{14}$ atoms cm^{-2}.

Since the rate of two-photon decays of a metastable beam at a fixed detector location is proportional to the metastable density, a large cross-section at a low energy is required for the maximum rate, and so the near resonant charge-exchange process is used here.

III.3.   Vacuum system.

The vacuum system consists of five main stainless steel vacuum chambers, individually pumped, Fig. 5.   These are designated, in order from the ion source,as, the lens chamber, the differential pumping chamber I, (DP I), the differential pumping chamber II, (DP II), the ultra high vacuum chamber I, (UHV I), and the ultra high vacuum chamber II, (UHV II).   All of the flanges on the UHV chambers are sealed with aluminium gaskets.   Most of the flanges on the rest of the system are sealed with Viton 'O' rings.

The lens chamber is pumped with a six-inch type EO6 oil diffusion pump, with a water-cooled chevron baffle to prevent backstreaming of the pump oil, and is isolated from the chamber by a quarter-swing butterfly valve.

The 600 l s^{-1} diffusion pump is backed by a type ES 330 334 l min^{-1}, oil sealed rotary pump. All the diffusion pumps in the system are filled with polyphenyl ether pumping fluid, (Santovac 5), with a vapour pressure in the 10^{-10} torr region, and is highly resistant to cracking. Cleaver et al.[49] found that under intense electron bombardment, this fluid gave rise to conducting films, and no evidence for the build up of insulating layers on the ion source or the lens system was found here.

Chamber DP I is evacuated by a two-inch EO-2 150 l s^{-1} oil diffusion pump and an ES50 50 l min^{-1} oil sealed backing pump, with thermoelectrically cooled chevron baffle and butterfly valve. Typical operating pressures in this chamber are 1 10^{-7} torr when the ion source is not running, and 1 10^{-6} torr with the source on.

The pumping stack attached to chamber DP II is similar to that on DP I, with the addition of a liquid nitrogen cold trap, as the pressure in this chamber was observed to be dominated by water vapour. Typical operating pressure in this chamber is 5 10^{-7} torr, the ion beam having little effect.

Between chambers DP I and UHV II, there is a pumping aperture, 20 mm long and 10 mm diameter, which also serves to collimate the beam. Chamber UHV I is pumped by a four-inch EO4 600 l s^{-1} oil filled diffusion pump, and an ES200 190 l min^{-1} oil sealed rotary backing pump, with thermoelectrically cooled chevron baffle and butterfly valve.

Chamber UHV II pumping stack consists of an E06/ES330 combination, as for the lens chamber, with thermoelectric baffle, liquid nitrogen cold trap, and butterfly valve. Both chambers UHV I and UHV II, being all metal gasket sealed, could be baked to $400^{\circ}C$ by means of convection heaters totalling 7 kW distributed beneath them. A double-walled aluminium baking jacket, with the cavity filled with ceramic fibre, which could be fitted completely over these two chambers with a slot at one end to allow the connection to DP II to pass through. After 24 hours baking at temperatures between 350° and $400^{\circ}C$, and with all the cold traps filled, the pressure in UHV I eventually reached $4.5 \ 10^{-9}$ torr, and in UHV II, $1 \ 10^{-9}$ torr. The presence of an ion beam had no detectable effect on the pressure in UHV I, and caused the pressure in UHV II to rise to about $2 \ 10^{-9}$ torr.

In all the chambers, the pressure is monitored by Bayard-Alpert type ionization gauges with X-ray limits of $2 \ 10^{-10}$ torr, and the vacuum composition could be monitored with a quadrupole mass spectrometer in UHV II.

III.4. Ion source.

The ion source is a Von Ardenne type duoplasmatron, munufactured by Edwards High Vacuum, and designed to produce high brightness, low emittance proton beams at energies less than 5 keV, Fig. 6.

Electrons are produced by a tantalum filament heated by a 15 V, 60 A ac supply, and an arc is struck between
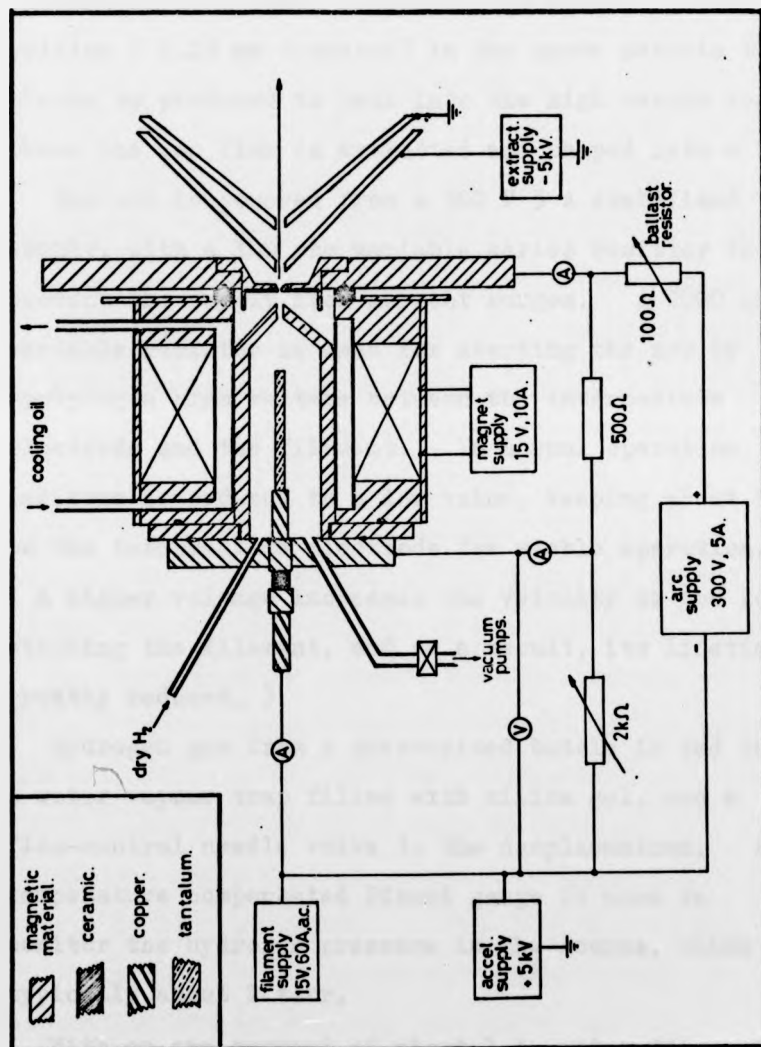
Fig. 6.

Ion source and power supplies.

the filament and anode.   An intermediate electrode
constructed of magnetic stainless steel constricts the
arc, which is focussed to a small area by a longitudinal
magnetic field, thus producing a high degree of
ionization in a small region at the anode.   A small
orifice (0.15 mm diameter) in the anode permits the
plasma so produced to leak into the high vacuum region
where the ion flux is extracted and shaped into a beam.

The arc is powered from a 300 V 5 A stabilised
supply, with a 100 ohm variable series resistor to
protect the supply from current surges.   A 2000 ohm
variable resistor is used for starting the arc by
applying a high voltage between the intermediate
electrode and the filament.   In normal operation, this
resistor is reduced to a low value, keeping about 30 V
on the intermediate electrode for stable operation.
(A higher voltage increases the velocity of the ions
striking the filament, and as a result, its lifetime is
greatly reduced.)

Hydrogen gas from a pressurised bottle is fed through
a water vapour trap filled with silica gel, and a
fine-control needle valve to the duoplasmatron.   A
temperature compensated Pirani gauge is used to
monitor the hydrogen pressure in the source, which is
typically about 1 torr.

With an arc current of about 1 A, and a filament
current of 50 A, the source ran with reasonable stability
for periods normally exceeding 100 hours, (limited by
the filament lifetime).

III.5.   Lens system and analysing magnet.

A double electrostatic lens system is used to extract, accelerate and focus the ion beam.   The first lens is an acceletate-decelerate gap lens, Fig. 6, which controls the primary beam divergence.   The second lens is a three-electrode decelerate-accelerate Einzel type, which controls the focus of the ion beam on target, without changing the beam energy.   A voltage of -90 V is permanently applied to the outer elements of the Einzel lens, which then act as electron repellers forcing electrons back into the beam to maintain space-charge neutralization.

A standard C-type electromagnet is used to seperate the different mass components of the beam.   The pole pieces are shaped to allow stigmatic focussing, so that the circular cross-section of the beam, and thus the maximum current density, can be maintained at the target.

The duoplasmatron produces the ion species, H_1^+ , H_2^+ , and H_3^+ in the approximate percentages of the total beam of, 20% , 40% , and 40% , respectively.   The proton beam is deflected through an angle of 30°, and a stainless steel bellows attached to chamber DP I assists in beam alignment.   Fig. 7 indicates how the proton current output varies with beam energy, as measured by the faraday cup in chamber UHV II.
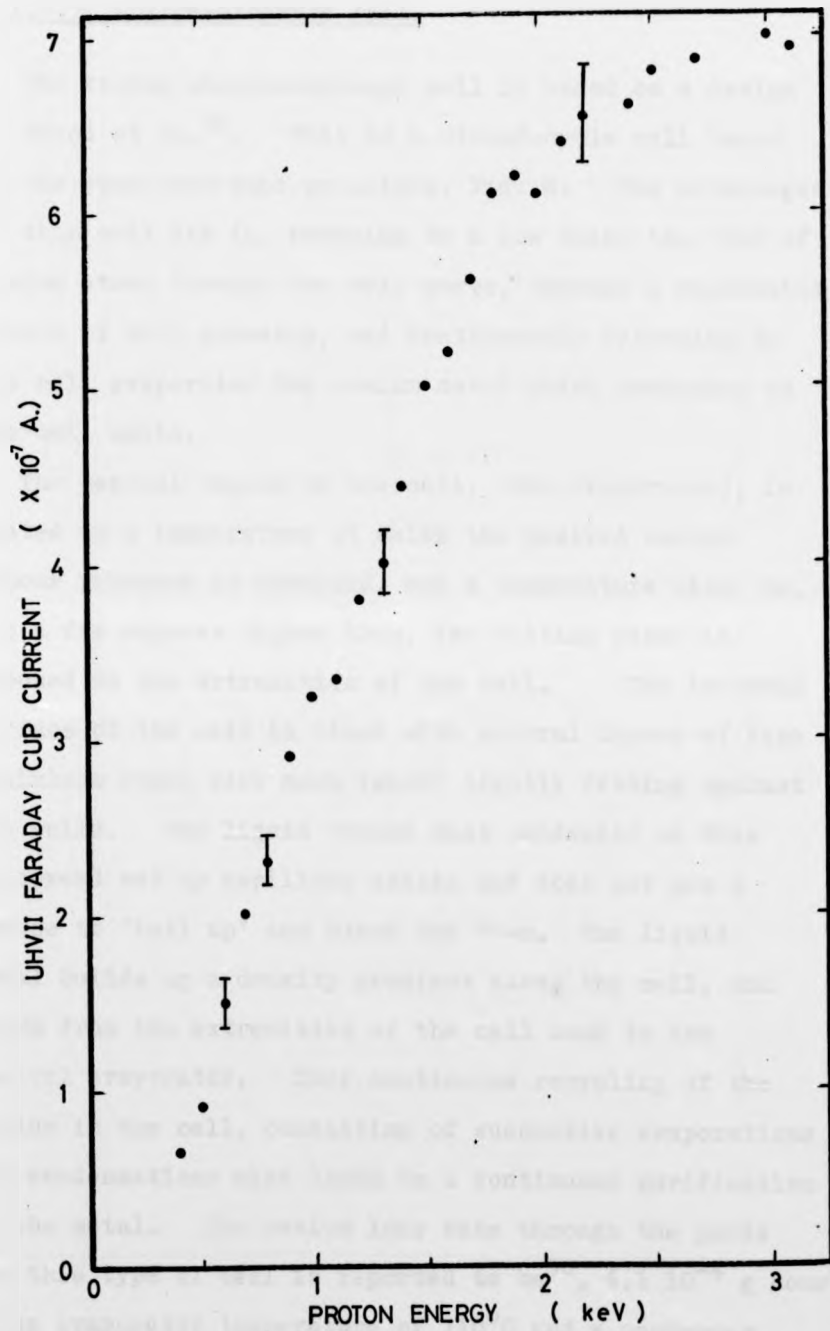
Fig. 7.

Proton output current versus beam energy. Error bars
show error estimated from repeated measurements.

III.6.1 Charge-exchange cell.

The cesium charge-exchange cell is based on a design of Bacal et al.[50]. This is a closed-cycle cell based on the open heat pipe principle, Fig. 8. The advantages of this cell lie in, reducing to a low value the flux of cesium atoms through the cell ports, through a reasonable choice of cell geometry, and continuously returning to the cell evaporator the cesium metal which condenses on the cell walls.

The central region of the cell, (the evaporator), is heated to a temperature at which the desired cesium vapour pressure is obtained, and a temperature close to, but a few degrees higher than, the melting point is imposed on the extremities of the cell. The internal surface of the cell is lined with several layers of fine stainless steel wire mesh (wick) tightly fitting against the walls. The liquid cesium that condenses on this is spread out by capillary action and does not get a chance to 'ball up' and block the beam. The liquid metal builds up a density gradient along the cell, and flows from the extremities of the cell back to the central evaporator. This continuous recycling of the cesium in the cell, consisting of successive evaporations and condensations also leads to a continuous purification of the metal. The cesium loss rate through the ports for this type of cell is reported to be[50], $6.1 \ 10^{-4}$ g hour^{-1}, at an evaporator temperature of 110°C and a condenser temperature of 32°C. Loss rates approaching this value have been observed here.
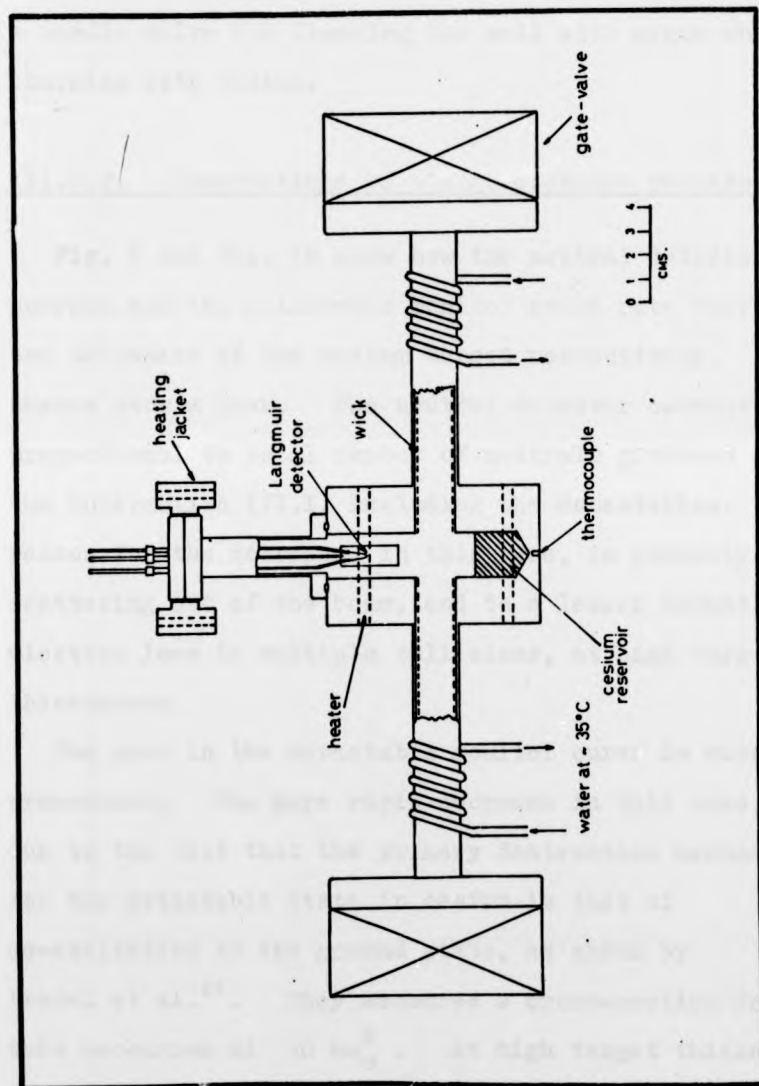
Fig. 8.

Cesium charge-exchange cell.

The cell can be isolated from the vacuum system by means of gate valves at either end, and has three auxillary ports, one supporting a Langmuir-Taylor hot-wire ionization detector, and another supporting a needle valve for flushing the cell with argon when charging with cesium.

III.6.2.   Observations of charge-exchange processes.

Fig. 9 and Fig. 10 show how the neutral detector current and the metastable monitor count rate vary with the thickness of the cesium target respectively.   Both curves show a peak.   The neutral detector current is proportional to total number of neutrals produced in the interaction III.1, including the metastables.   The reason for the decrease, in this case, is probably scattering out of the beam, and to a lesser extent, electron loss in multiple collisions, at high target thicknesses.

The peak in the metastable monitor curve is much more pronounced.   The more rapid decrease in this case, is due to the fact that the primary destruction mechanism for the metastable state in cesium is that of de-excitation to the ground state, as shown by Pradel et al.[36].   They measured a cross-section for this mechanism of $50 \, \pi a_o^2$.   At high target thicknesses, where multiple collisions occur, almost all the metastables produced are also de-excited.   The shapes of these curves, Fig 9 and Fig. 10, agree quite well with the observations of Pradel et al.[36], and
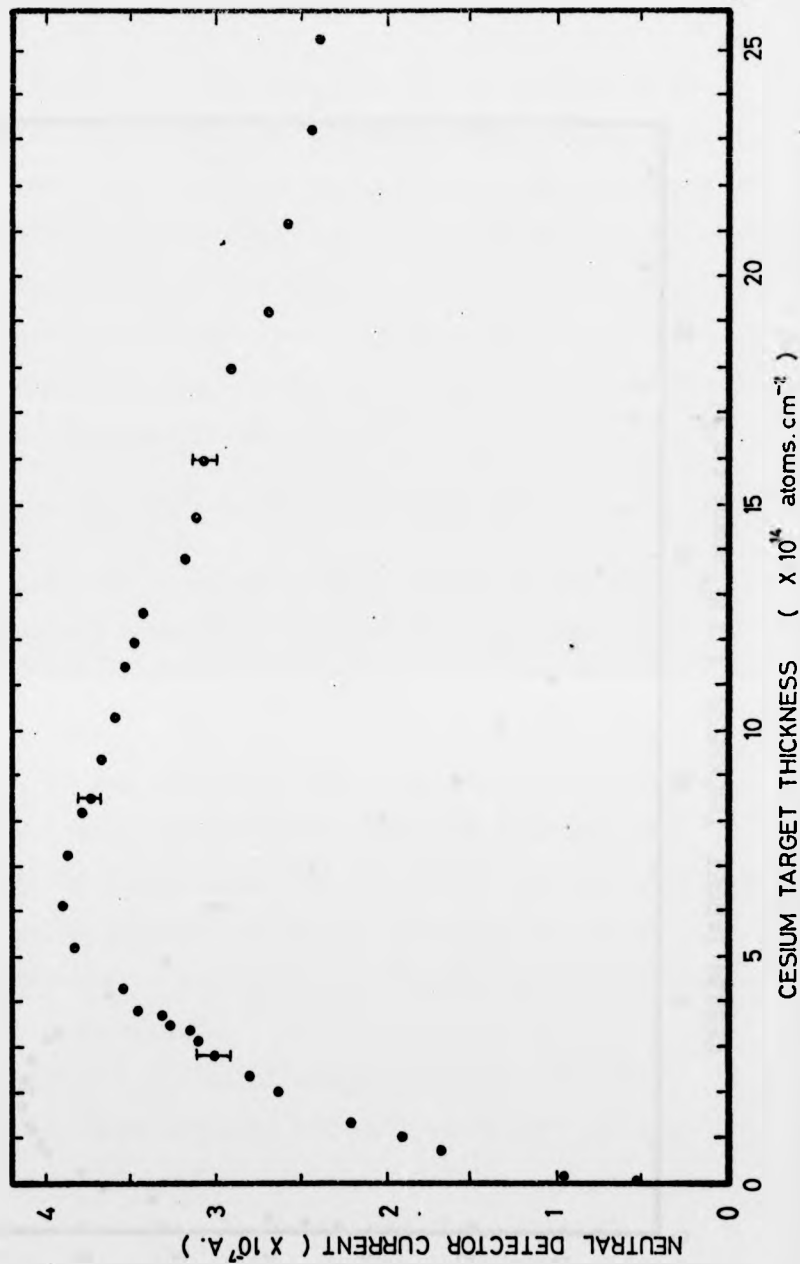
Fig. 9.

Total neutrals produced versus cesium target thickness.
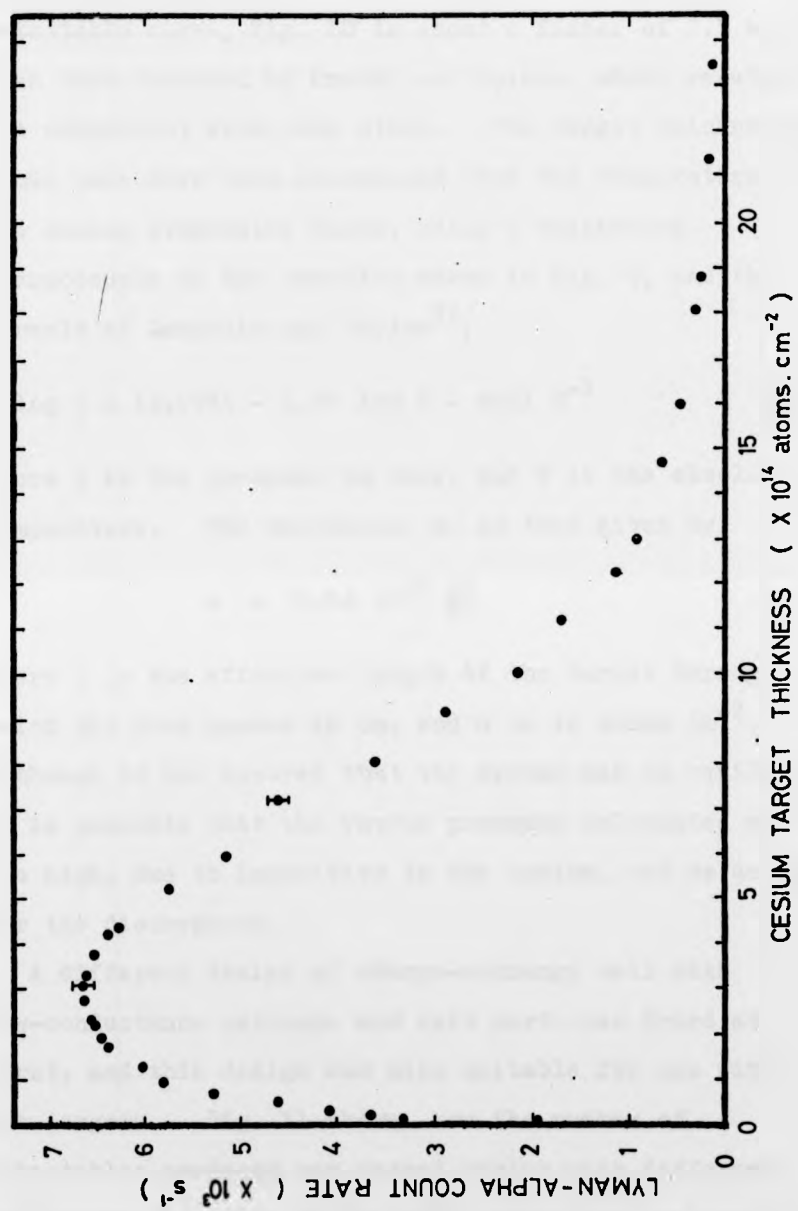Error bars show error estimated from fluctuations
due to beam instabilities.

Fig. 10.

Metastable flux versus cesium target thickness.
Error bars show one standard deviation.

Spiess et al.[34].   The position of the maximum in the
metastable curve, Fig. 10 is about a factor of 2.5 higher
than that observed by Pradel and Spiess, whose results
are consistent with each other.   The target thicknesses
shown here have been calculated from the temperature of
the cesium evaporator block, using a calibrated
thermocouple at the position shown in Fig. 8, and the
formula of Langmuir and Taylor[52],

$$\log p = 11.0531 - 1.35 \log T - 4041 \, T^{-1} \qquad \text{III.2.}$$

where p is the pressure in torr, and T is the absolute
temperature.   The thickness, π, is then given by,

$$\pi = 9.64 \; 10^{18} \; \frac{pl}{T} \qquad \text{III.3.}$$

where l is the effective length of the target through
which the beam passes in cm, and π is in atoms cm^{-2}.
Although it was ensured that the system was in equilibrium,
it is possible that the vapour pressure calculated was
too high, due to impurities in the cesium, and so account
for the discrepancy.

   A different design of charge-exchange cell with
low-conductance entrance and exit ports was tried at
first, and this design was also suitable for use with
gas targets.   Fig. 11 shows how the number of
metastables produced per second varies with different
thicknesses of argon in the cell. Argon, at low energies, has a
relatively large cross-section for metastable production,
about 0.1 πa_o^2 , compared with that of molecular hydrogen,
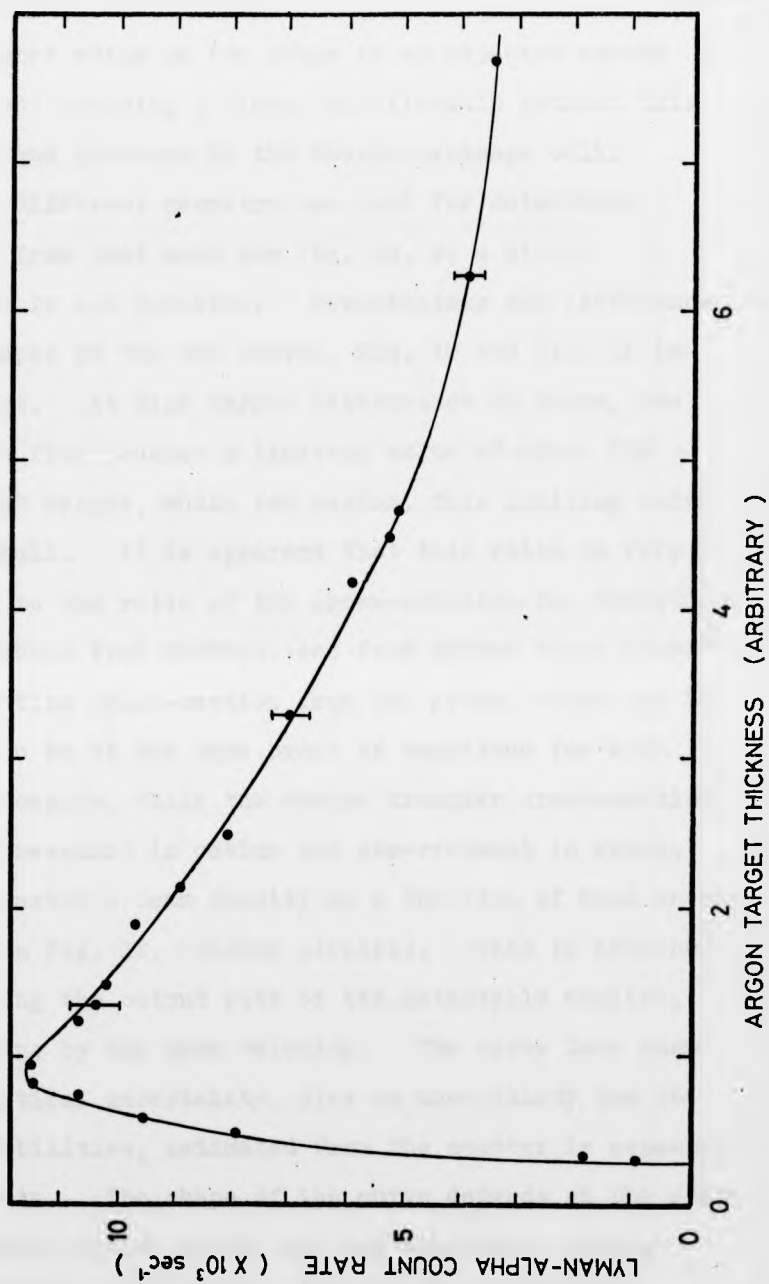which has about 0.01 πa_o^2 [45].   The target thickness here

Fig. 11.

Metastable flux (relative) versus argon target thickness.
Error bars show statistical error plus error due
to instabilities.

was monitored using an ion gauge in an adjacent vacuum
chamber, and assuming a linear relationship between this
and the argon pressure in the charge-exchange cell.
However a different geometry was used for metastable
detection from that used for Fig. 10, so a direct
comparison is not possible.   Nevertheless the difference
in the shapes of the two curves, Fig. 10 and Fig. 11 is
of interest.   At high target thicknesses in argon, the
metastable flux reaches a limiting value of about 25%
of the peak height, while for cesium, this limiting value
is very small.   It is apparent that this ratio is very
sensitive to the ratio of the cross-sections for formation
of metastables from protons, and from ground state atoms[55].
The excitation cross-section from the ground state can be
expected to be .of the same order of magnitude for both
argon and cesium, while the charge transfer cross-section
is nearly resonant in cesium and non-resonant in argon.

The metastable beam density as a function of beam energy
is shown in Fig. 12, (closed circles).   This is obtained
by measuring the output rate of the metastable monitor,
and dividing by the beam velocity.   The error bars show
the statistical uncertainty, plus an uncertainty due to
beam instabilities, estimated from the scatter in repeated
measurements.   The shape of the curve depends on the shape
of the cross-section curve, and the ion source proton
output versus energy curve, Fig. 7.   The metastable
density displays a maximum at about 1.1 keV.

The neutral detector output current is also shown in
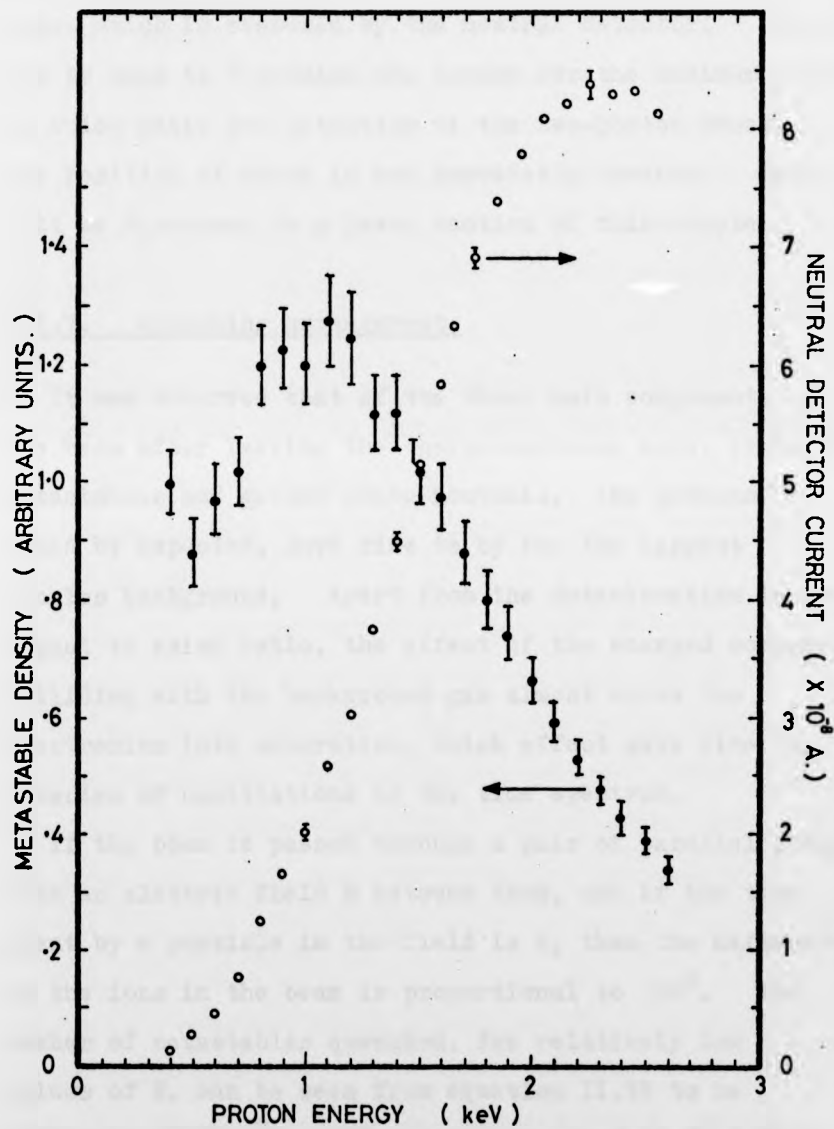Fig. 7, the error bars showing the estimated error due to

Fig. 12.

Metastable beam density (closed circles) and total
neutral flux (open circles) versus beam energy,
error bars show statistical error plus error due
to instabilities.

the scatter in repeated measurements. The main
contribution to the random background in the coincidence
time spectrum, when the charged component has been
removed, is from the neutral current through the quartz
tube, which is measured by the neutral detector. Fig. 12
can be used to determine the energy for the maximum signal
to noise ratio for detection of the two-photon decay,
the position of which is not immediatly obvious. This
will be discussed in a later section of this chapter.

III.7. Quenching arrangement.

It was observed that of the three main components of
the beam after leaving the charge-exchange cell, protons,
metastables and ground state neutrals, the protons, as
would be expected, gave rise to by far the largest
singles background. Apart from the deterioration in the
signal to noise ratio, the effect of the charged component
colliding with the background gas almost drove the
electronics into saturation, which effect gave rise to
a series of oscillations in the time spectrum.

If the beam is passed through a pair of parallel plates
with an electric field E between them, and if the time
spent by a particle in the field is t, then the deflection
of the ions in the beam is proportional to Et^2. The
number of metastables quenched, for relatively low
values of E, can be seen from equation II.38 to be
proportional to E^2t. It can be seen that if t is made
large enough and E small enough, it is possible to
remove all the ions from the beam without quenching

an appreciable number of metastables.   These conditions
are satisfied by a long pair of plates, with a low electric
field applied.   In the present experiment, the length
of the charge removal plates is limited by the size of
the vacuum tanks.   A pair of plates of length 60 mm,
and a spacing of about 40 mm were employed, which also
serve as pre-quench plates for the metastable component.

With a pure proton beam passing through the apparatus,
it was found that 99.95% approximately of the beam was
restricted from entering the quartz tube at an applied
voltage of $\pm$ 45 V.   Fig. 13 shows how the metastable
monitor count rate varies with the voltage applied to
the pre-quench plates.   It can be seen that at $\pm$ 45 V,
about 27% of the metastables are quenched.   Although
these figures could be greatly improver upon, they were
found acceptable.

In Fig. 13, the points are the measured values, the
error bars show one standard deviation, and the solid
line is the calculated curve for the remaining fraction
of metastables after passing through the pre-quench
plates with a voltage V applied.   It is easily shown
from equation II.38, that the remaining fraction is,

$$ f = e^{-kV^2} \qquad\qquad III.4. $$

where k is a constant which depends on the beam velocity
and the plate geometry.   The value of k used here is
chosen for the best fit to the measured points, and is,

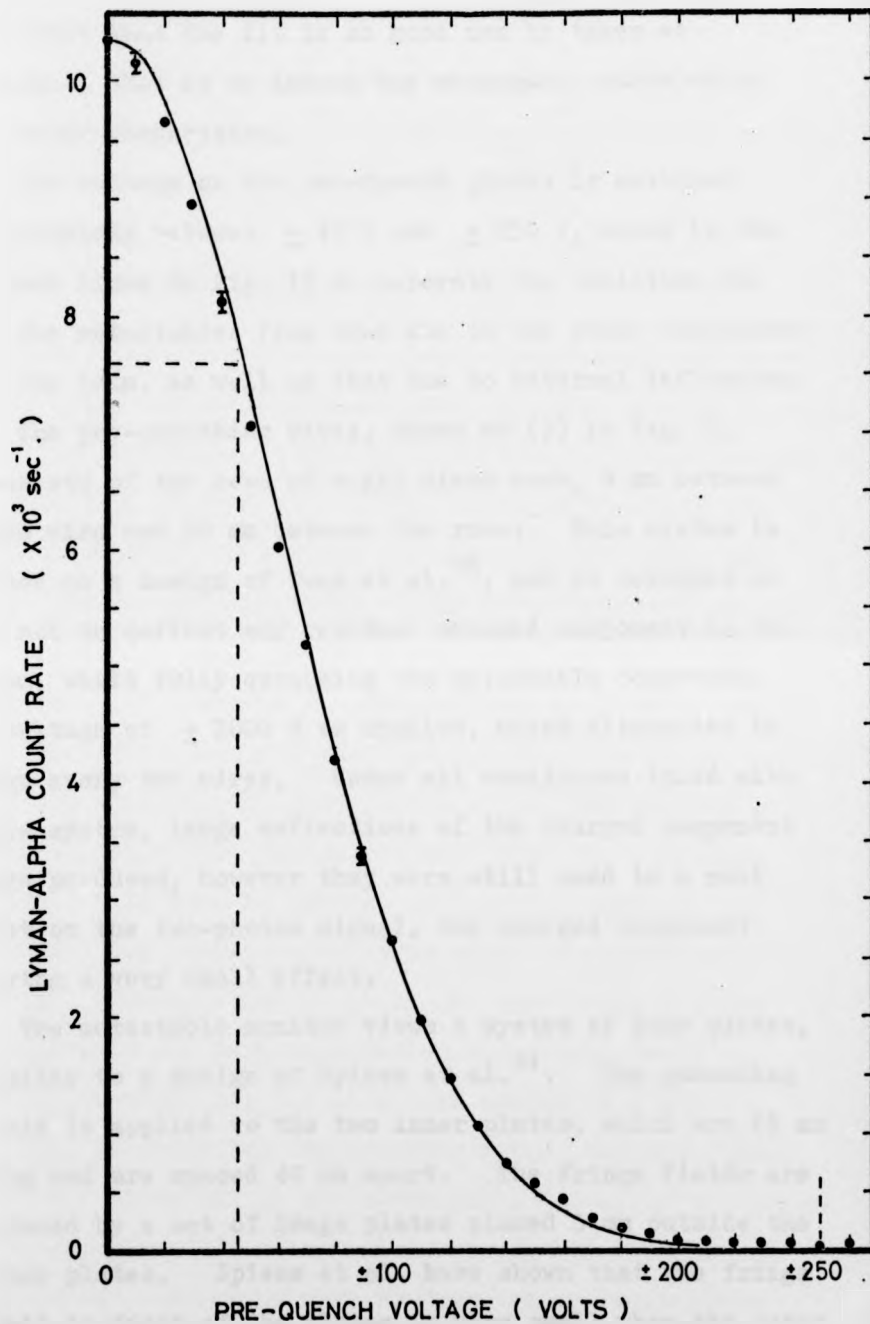$$ k = 1.374 \ 10^{-4} \ V^{-2} $$

Fig. 13.

Lyman-alpha count rate versus pre-quench plate voltage.
Points are the measured values, the solid curve is
fitted using equation III.4.
Error bars show one standard deviation.

The fact that the fit is so good can be taken as evidence that it is indeed the metastable state which is under observation.

The voltage on the pre-quench plates is switched alternately between $\pm$ 45 V and $\pm$ 250 V, shown by the dashed lines in Fig. 13 to seperate the radiation due to the metastables from that due to the other components of the beam, as well as that due to external influences.

The pre-quenching wires, shown at (9) in Fig. 5, consists of two rows of eight wires each, 8 mm between each wire and 20 mm between the rows. This system is based on a design of Tuan et al.[56], and is designed so as not to deflect any residual charged component in the beam, while fully quenching the metastable component. A voltage of $\pm$ 1000 V is applied, which alternates in sign every two wires. Under all conditions tried with this system, large deflections of the charged component were produced, however they were still used in a null test on the two-photon signal, the charged component giving a very small effect.

The metastable monitor views a system of four plates, similar to a design of Spiess et al.[34]. The quenching field is applied to the two inner plates, which are 65 mm long and are spaced 40 mm apart. The fringe fields are reduced by a set of image plates placed 3 mm outside the inner plates. Spiess et al. have shown that the fringe field in front of the plates is very small when the outer plates are 4 mm longer than the inner ones, and so it will not appreciably influence the metastable beam in the

detection region.   Fig 14 is a plot of the Lyman-alpha
photomultiplier output against the voltage applied to
the quench plates, with a metastable beam passing through.
The normal operating voltage is $\pm$ 500 V.

III.8.   Neutral detector.

The neutral detector consists of a faraday cup, with
guard ring and a 90% transparency tungsten wire mesh over
the cup enterance. With the guard ring and mesh biassed
negatively, it operates as an electron-suppressed faraday
cup,to measure the charged component of the beam, and
with the charged component of the beam deflected by the
quench field, and a positive potential on the guard ring
and mesh, it measures the neutral component of the beam.
The secondary electrons emitted by the neutrals on striking
the cup surface, are accelerated out of the cup and give
rise to a positive current flowing from the detector,
which can be used to measure the neutral current,
provided the secondary electron emission coefficient is
known.   Pradel et al.[35] found the same value for the
coefficient for both metastables and ground state
neutrals, which is, 1.7 at a beam energy of 1 keV.

Fig. 15 shows how the detector output current varies
with the potential on the guard ring, (actually the guard
ring was grounded and a negative potential applied to
the cup).   It can be seen to approach an equilibrium
value only after about 40 V is applied.   This implies
that the secondary electron energy spread extends to this
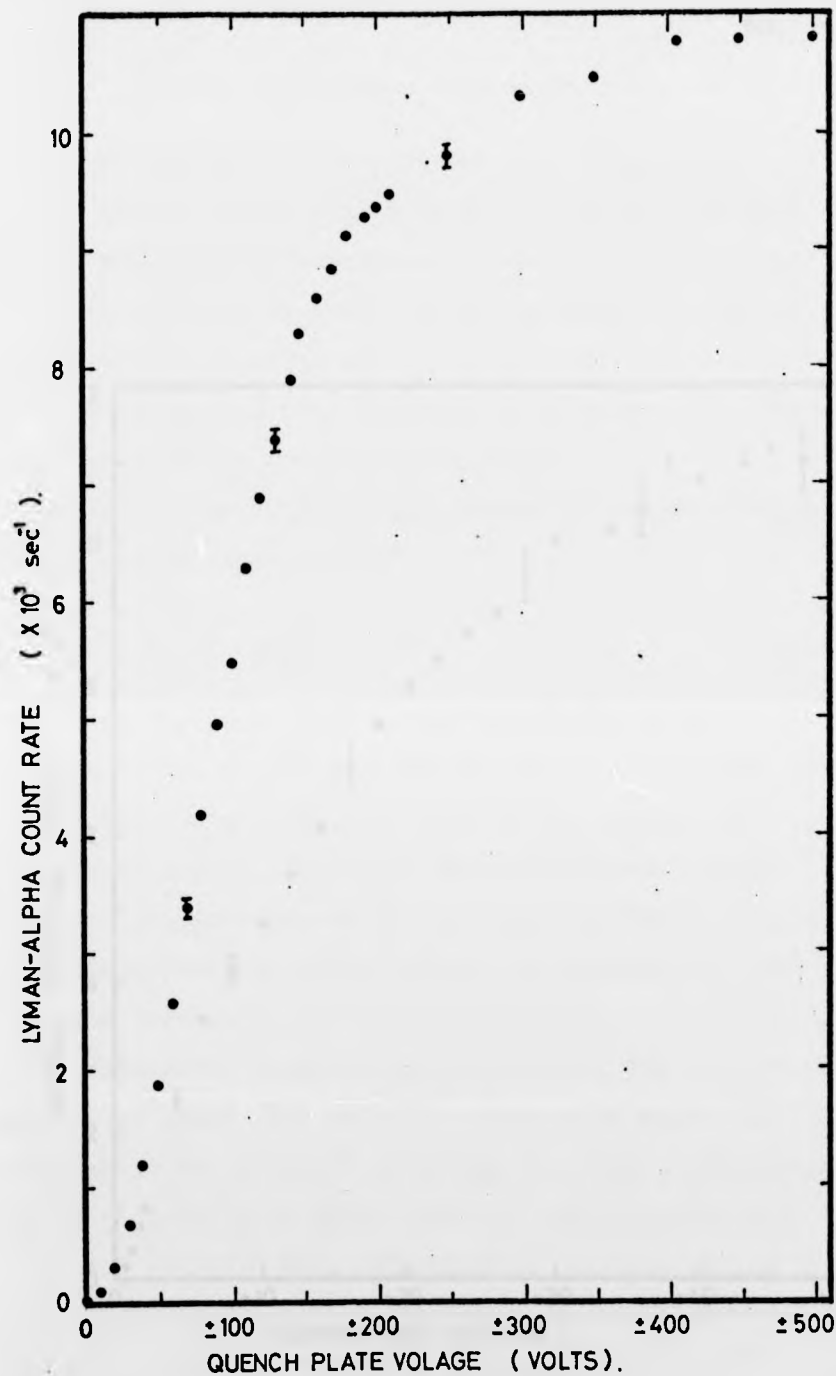value.   The normal operating guard ring voltage is 45 V.

Fig. 14.

Lyman-alpha count rate versus quench plate voltage.

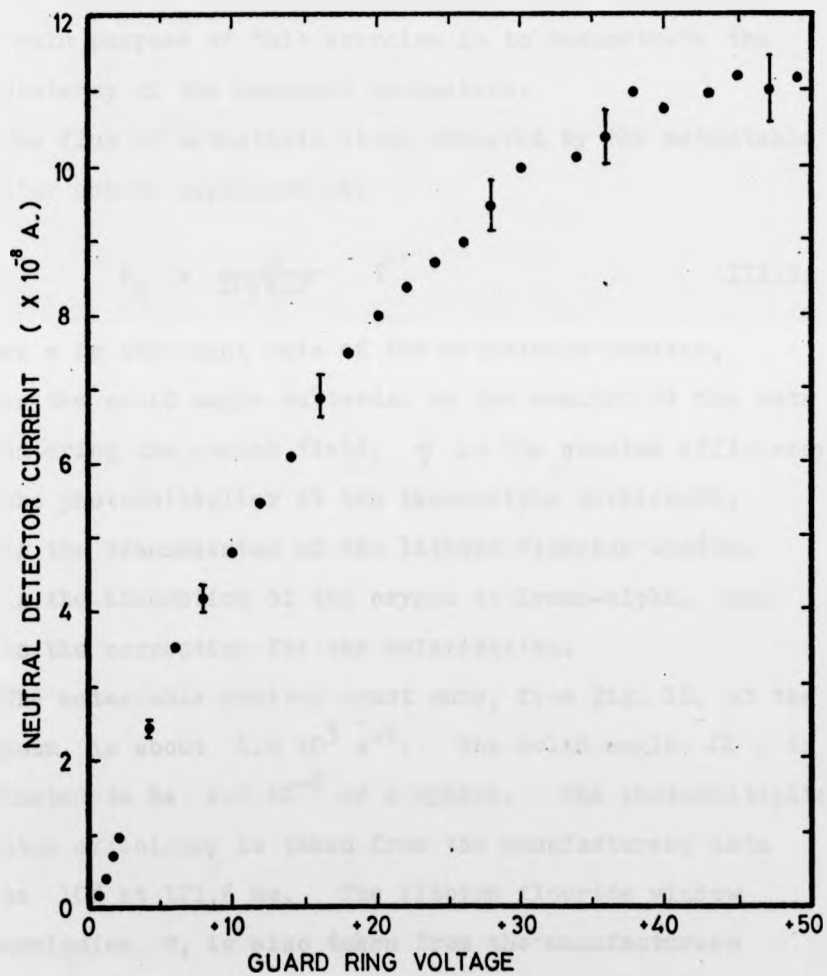Error bars show one standard deviation.

Fig. 15.

Neutral detector output current versus guard ring
voltage, for a constant beam. Error bars are estimated
from scatter in repeated measurements.

III.9.   Estimate of the beam composition.

A rough estimate of the neutral beam composition will be made at the cesium target thickness which gives the maximum number of metastables.   It must be emphasised that this can only be a very crude estimate for some of the quantities required are not known very accurately. The main purpose of this exercise is to demonstrate the consistency of the measured parameters.

The flux of metastable atoms observed by the metastable monitor can be expressed as,

$$F_m = \frac{n}{\Omega \eta T a P} \quad s^{-1}$$
III.5.

where n is the count rate of the metastable monitor, Ω is the solid angle subtended by the monitor at the beam on entering the quench field, η is the quantum efficiency of the photomultiplier at the Lyman-alpha wavelength, T is the transmission of the lithium flouride window, a is the absorbtion of the oxygen at Lyman-alpha, and P is the correction for the polarization.

The metastable monitor count rate, from Fig. 10, at the maximum, is about 6.6×10^3 s^{-1}.   The solid angle, Ω , is estimated to be 6.5×10^{-5} of a sphere.   The photomultiplier quantum efficiency is taken from the manufacturers data to be 10% at 121.6 nm.   The lithium flouride window transmission, T, is also taken from the manufacturers data to be 50% at the same wavelength. The absorbtion coefficient of dry molecular oxygen at atmospheric pressure at the Lyman-alpha wavelength is

given by Carriere and de Heer[57] as 0.7 cm^{-1}. Since the length a photon has to travel through the oxygen is about 4 cm, its transmission is about 6% .

It is well known that the radiation emitted by metastable atoms in an electric field is anisotropic[58]. The measurements of Wijngaarden et al.[58], extrapolated to a field strength of 250 V cm^{-1}, the value of the quench field used here, give the anisotropy, R as about 0.168. The anisotropy is defined as,

$$R = \frac{I_{\parallel} - I_{\perp}}{I_{\parallel} + I_{\perp}} \qquad \text{III.6.}$$

where $I_{\parallel}$ and $I_{\perp}$ are the intensities measured in the directions parallel to, and perpindicular to, the field lines respectively. The intensity measured here is $I_{\perp}$, and so we have,

$$\frac{I_{\perp}}{I_{\parallel} + I_{\perp}} = \frac{1 - R}{2} = 0.416$$

i.e., the value measured here is too small by a factor of 0.416.

Combining these results, we get the metastable flux as,

$$F_m = 8.1 \; 10^{10} \quad H(2S) \; s^{-1} .$$

The flux of neutral atoms is given by,

$$F_g = \frac{i_{nd}}{e \gamma} \qquad \text{III.7.}$$

where i_{nd} is the current from the neutral detector, e is the electronic charge, and γ is the secondary electron emission coefficient. Pradel et al.[35] have measured γ for 'dirty' stainless steel as about 1.7 for a neutral

beam energy of 1 keV. At the cesium thickness at which
the metastable flux is at a maximum, (about $3 \ 10^{14}$ atoms cm^{-2})
the neutral detector current is about $3.1 \ 10^{-7}$ A, from
Fig. 9. These values give the total neutral flux as,

$$F_g = 1.1 \ 10^{12} \text{ atoms } s^{-1}.$$

which gives,

$$F_m/F_g = 0.074 \quad \text{or} \quad 7.4\% \ .$$

The maximum percentage of metastables in the neutral
beam measured by Pradel et al.[35] was about 30%, with a
similar experimental arrangement. Bearing in mind the
large uncertainties in most of the parameters used above,
the agreement is not bad.

III.10.1.   Detection arrangement.

Between chambers UHV I and II is mounted a vacuum-tight
tube of synthetic quartz, (Spectrosil). Around this
tube is fixed a light-tight and reasonably air-tight
aluminium box. Fixed to one side of the box is a
turntable assembly, consisting of a rotor inside a stator
through which the quartz tube passes. One detector
(photomultiplier tube) can be mounted on the rotor, and
another on the stator, so that the angular distribution
of the coincidences can be investigated. The whole
turntable and its associated drive assembly is designed
to fit inside chamber UHV II.

Synthetic quartz has a short-wavelength cut-off of
about 160 nm, which allows about 56% of the two-photon
spectrum to be observed. Since molecular oxygen begins

absorbing light at about 180 nm, it is desirable to
remove it from the detection region.   This can be achieved
by flushing the detector box with argon.

III.10.2.   Photomultiplier tubes.

    The main selection criteria for selecting the coincidence
photomultiplier tubes were the spectral response, and the
timing accuracy.   The spectral response was chosen to
peak at 240 nm, - half the Lyman-alpha frequency, for
both tubes.

    The coincidence photomultiplier tubes used in producing
the present results were an E.M.I. type 9816QB and a
Phillips type XP1023.
The 9816QB has a spectral response extending from 160 nm
to 750 nm, (S20), a peak quantum efficiency of 28%, an
anode pulse risetime of 2.3 ns, and a transit time difference
of 0.9 ns for electrons leaving the centre and a point
18 mm from the centre, of the photocathode.   The
photocathode diameter is 50 mm.

    The XP1023 has an S13 type spectral response, extending
from 160 nm to 620 nm, a peak quantum efficiency of 25%,
an anode pulse risetime of 1.8 ns, a transit time difference
of 0.2 ns, for the same conditions as the 9816QB, and
a photocathode diameter of 42 mm.

    Both coincidence photomultiplier tubes were housed
in 3 mm thick brass tubes to reduce spurious coincidences.

    An EMR type 542G-08-18 photomultiplier tube was
used as a Lyman-alpha monitor.   This tube is solar blind
with a lithium flouride window, and a spectral response

extending from 105 nm to 220 nm, peaking at the
Lyman-alpha wavelength of 121.6 nm.   A copper gasket
sealed lithium flouride window was mounted on chamber
UHV II , and a flowing dried molecular oxygen filter was
used between it and the photomultiplier as a Lyman-alpha
filter.   It is well known that molecular oxygen has a
transmission window at this wavelength[57].

III.11.1.   Electronics.

The electronic system is designed to have the best
practical timing resolution, so matched 50 ohm cables
are used throughout, and great care was taken to match
the photomultiplier anodes to the cable.   Although
dc-coupled amplifiers and discriminators are used, it
was felt desirable to operate the photocathodes at ground
potential to avoid stray electric fields in the
detection region.   In consequence, the photomultiplier
anodes had to be ac-coupled, however no evidence for
pulse pile-up on the blocking capacitors was observed.

Initial operation of the detection system gave rise
to a number of spurious coincidence peaks, but most of
these were tracked down to either cross-talk between the
coincidence channels, or electrical pick-up.   After
these effects had been eliminated, however, a small
spurious coincidence peak still remained, which, after
a number of tests were made, was ascribed to cosmic rays.
Similar effects have been observed by Novick[59], and
King et al.[60].

The solution adopted to eliminate this effect was
to modulate the metastable component of the beam,
using a dc electric quenching field, and synchronously
switching the detection system.   Although this completely
eliminated the spurious effect, it also doubled the
measurement period.

A schematic diagram of the electronic system is shown
in Fig. 16.   The anode pulses from the coincidence
photomultipliers are amplified by a factor of 10 in
fast amplifiers, type NE4634, which have a risetime of
about 2 ns.   The output pulses are fed to constant
fraction of pulse height timing discriminators, ORTEC
type 463.   One of the discriminator outputs is taken
directly to the start input of an ORTEC type 447 time-
to-pulse-height converter (TAC), while the other is
taken through a variable delay unit, to the stop input.
The TAC produces an output pulse whose amplitude is
proportional to the arrival time difference of the start
and stop pulses.   The TAC linearity is optimum in the
centre of its timing range,so the variable delay is
adjusted to position the true coincidence peak in this
region.   The TAC output is gated off by a switch unit
when the voltage on the proton removal (pre-quench) plates
is being changed, to avoid the possibility of spurious
coincidences being generated.

The TAC output is taken directly to the input of a
multi-channel pulse height analyser (MCPHA), an Intertechnique
DIDAC 800.   The subgroup of the MCPHA memory that is
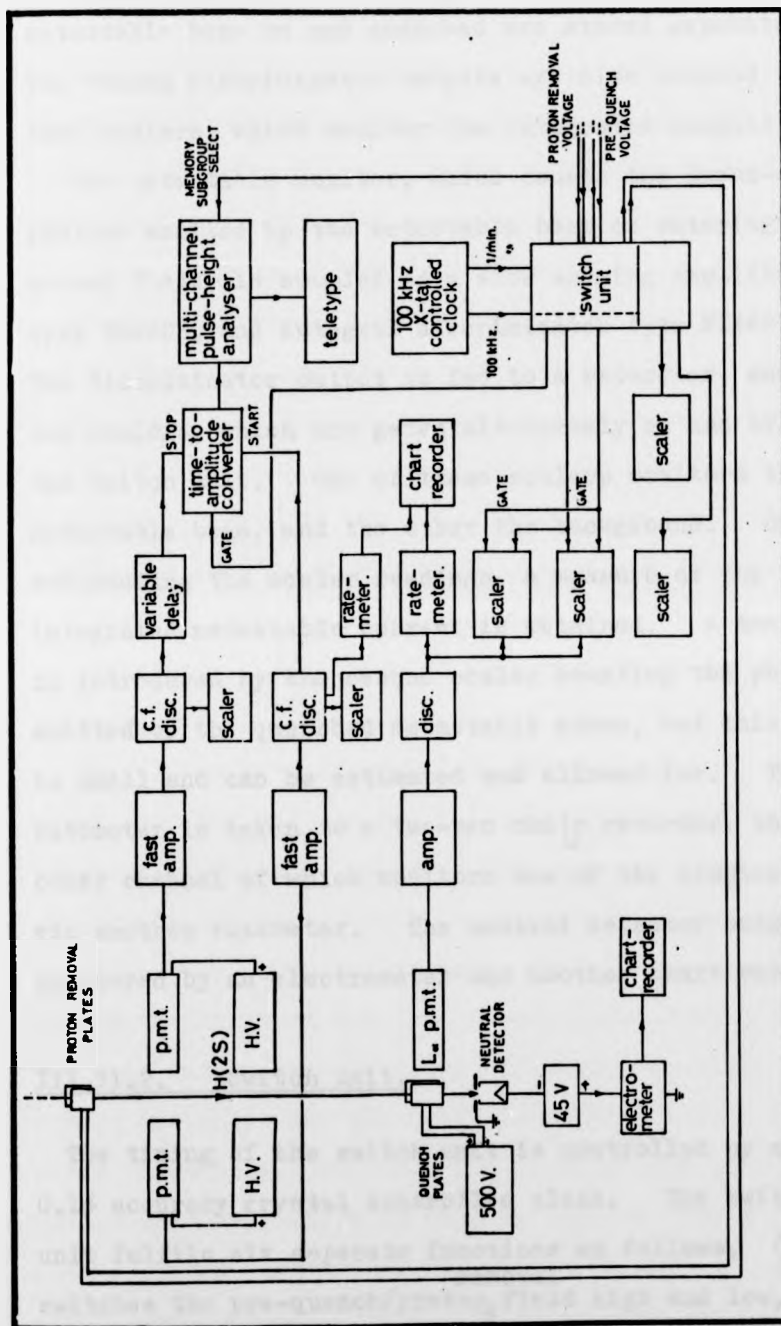being addressed by the TAC output is also determined by

Fig. 16.

Schematic diagram of electromic system.

the switch unit, so that the time spectra for the
metastable beam on and quenched are stored seperately.
The timing discriminator outputs are also coupled to
fast scalers, which monitor the integrated singles counts.

The metastable monitor, which counts the Lyman-alpha
photons emitted by the metastable beam on entering the
quench field, is coupled to a slow shaping amplifier,
type NE4603, and integral discriminator type NE4623.
The discriminator output is fed to a ratemeter, and
two scalers, which are gated alternately on and off by
the switch unit.   One of these scalers monitors the
metastable beam, and the other the background.   On
subtracting the scaler readings, a measure of the
integrated metastable current is obtained.   A small error
is introduced by the second scaler counting the photons
emitted by the quenched metastable atoms, but this effect
is small and can be estimated and allowed for.   The
ratemeter is taken to a two-pen chatr recorder, the
other channel of which monitors one of the singles rates
via another ratemeter.   The neutral detector output is
monitored by an electrometer and another chart recorder.

III.11.2.   Switch unit.

The timing of the switch unit is controlled by a 100 kHz,
0.1% accuracy crystal controlled clock.   The switch
unit fulfils six seperate functions as follows, (1), it
switches the pre-quench/proton removal field high and low, (2), it
routes the metastable monitor output to one of two scalers,

depending on whether the pre-quench field is high or low, (3), it routes the TAC output to the appropriate subgroup of the multi-channel analyser memory, (4), it continuously monitors the timing of the high/low periods, (5), it gates the TAC off during a pre-quench field switching operation, for a precise amount of time, (0.655s), and (6), it switches the read/store function of the MCPHA.

The clock unit divider is normally set to produce one output pulse per minute, and the arrival of one of these ₢pulses at the switch unit initiates a change in level of the pre-quench field, provided the start button has been pressed. If the stop button is pressed during a run, the unit only changes to a stop condition when a switching cycle is complete, thus preserving equal on-off times irrespective of when the run was started or stopped.

Fig. 17 shows a schematic of the switch unit. The start and stop buttons are followed by an 'anti-bounce' circuit, (R-S latch), whose output goes to logic '1' when the start button is pressed, and to a logic 'O', when the stop button is pressed. This output is fed to the 'data' input of a D-type latch, whose output follows the data input when the clock (CK) input is high, and stores the data when the clock input goes low. The clock input is derived from the leading edge of the gating waveform, which in turn is derived from a J-K flip-flop, so that the latch outputs (Q and $\bar{Q}$) change state, -when demanded by the start and stop buttons,- at the beginning or end of a complete switching cycle. The
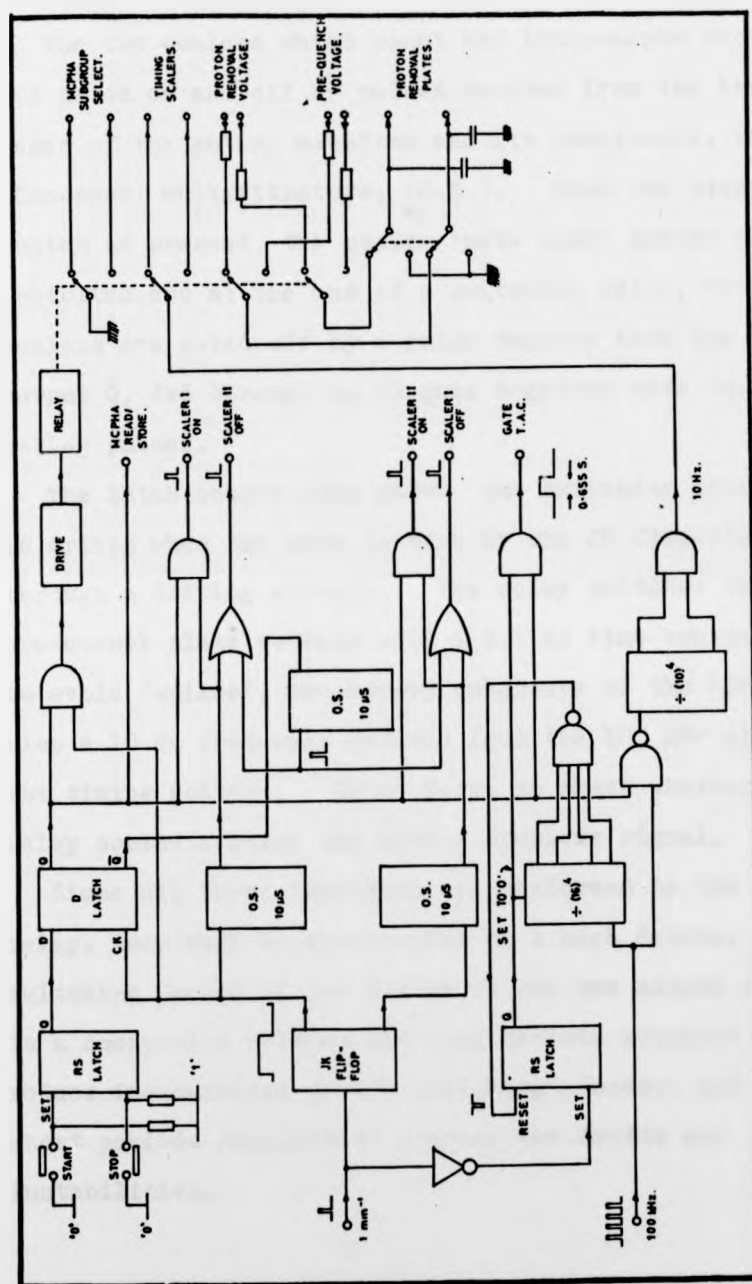
Fig. 17.

Schematic diagram of switch unit.

rest of the circuitry is then controlled by the latch outputs.

The two scalers which count the Lyman-alpha photons are geted on and off by pulses derived from the leading edges of the gating waveform and its complement, via 'One-shot' multivibrators, (O.S.). When the stop button is pressed, the scaler 'gate open' pulses are inhibited and at the end of a switching cycle, both scalers are gated off by a pulse derived from the latch output $\bar{Q}$, fed through an OR gate together with the normal gating pulses.

The latch output also gates the switching relay, which is driven when the gate is open by the JK flip-flop, through a driving circuit. The relay switches the pre-quench plate voltage with a 0.2 us time constant to avoid 'spikes', the memory subgroups of the MCPHA, and also a 10 Hz frequency derived from the 100 kHz clock, to the timing scalers. These serve to check whether the relay contacts stick and give a spurious signal.

Since all these functions are performed by the same relay, they must be synchronous to a high degree. The switching period of one minute on and one minute off, is a compromise between the long periods required to reduce inaccuracies in the switching process, and the short periods required to average out drifts and instabilities.

III.12. Light pulser.

To locate the zero position in the time spectrum, all
the relative delays associated with the two coincidence
channels must be known, or measured.   A fast pulse
generator is of limeted use, since no account is taken
of the different transit times in the photomultipliers.
A pulsed light source, if fast enough, measures all the
relative delays, as well as the time resolution.   An
ordinary visible light emitting diode (LED) is used here,
driven at a high current by a fast pulse.   The pulse
generator used is unusual, and is discussed below.

If the collector-base junction of a transistor is
reverse biassed with a sufficiently high voltage, the
minority carriers are accelerated across the depletion
region , causing ionization to occur by liberating bound
electrons, and setting up a micro-plasma in the base region[61].
This effect is called avalanche breakdown, and gives
rise to a negative resistance characteristic, which can
be utilised to produce fast risetime pulses.
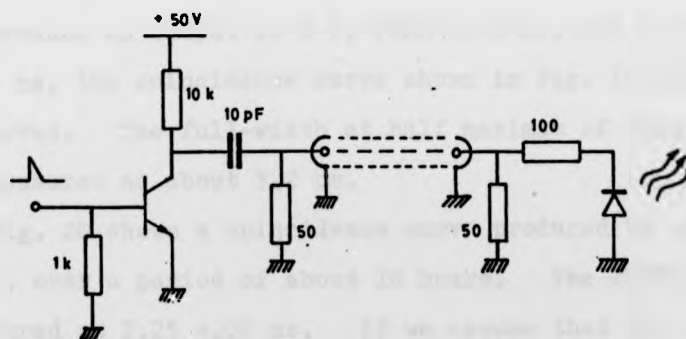
The circuit used here is shown in Fig. 18.

Fig. 18.

A positive pulse, derived·from a differentiated
multivibrator output, of amplitude about 2 V is applied
directly to the base.   The transistor turns on rapidly,
and avalanche breakdown is initiated.   The collector
voltage drops very rapidly, (the large value of the
collector resistor prevents the transistor from destroying
itself), and when the output capacitor has discharged
itself through the load, the transistor recovers, ready
for the next driving pulse.   The transistor is run at
a rate of about 1 kHz to avoid overheating.

With an ordinary type V405A silicon planar transistor,
and careful construction, an output of amplitude 28 V,
full-width at half maximum (FWHM) of 1 ns, and a risetime,
which was limited by the sampling oscilloscope used,to
0.35 ns.

The LED used was a Fairchild type FLVio , with a quoted
light output risetime of 10 ns.   By driving the LED at
a much higher forward current than the manufacturers
recommended maximum for a very short period, risetimes
much shorter than the quoted figure can be achieved.   If
the LED driving pulse is too short in duration, no light
output is observed.   With the pulse generator modified
to produce an output of 8 V, FWHM of 2 ns, and a risetime
of 1 ns, the coincidence curve shown in Fig. 19 was
observed.   The full-width at half maximum of this curve
is measured as about 3.2 ns.

Fig. 20 shows a coincidence curve produced by cosmic
rays, over a period of about 18 hours.   The FWHM here is
measured as 2.25 $\pm$.02 ns.   If we assume that the cosmic

A positive pulse, derived·from a differentiated multivibrator output, of amplitude about 2 V is applied directly to the base. The transistor turns on rapidly, and avalanche breakdown is initiated. The collector voltage drops very rapidly, (the large value of the collector resistor prevents the transistor from destroying itself), and when the output capacitor has discharged itself through the load, the transistor recovers, ready for the next driving pulse. The transistor is run at a rate of about 1 kHz to avoid overheating.

With an ordinary type V405A silicon planar transistor, and careful construction, an output of amplitude 28 V, full-width at half maximum (FWHM) of 1 ns, and a risetime, which was limited by the sampling oscilloscope used, to 0.35 ns.

The LED used was a Fairchild type FLVIO , with a quoted light output risetime of 10 ns. By driving the LED at a much higher forward current than the manufacturers recommended maximum for a very short period, risetimes much shorter than the quoted figure can be achieved. If the LED driving pulse is too short in duration, no light output is observed. With the pulse generator modified to produce an output of 8 V, FWHM of 2 ns, and a risetime of 1 ns, the coincidence curve shown in Fig. 19 was observed. The full-width at half maximum of this curve is measured as about 3.2 ns.

Fig. 20 shows a coincidence curve produced by cosmic rays, over a period of about 18 hours. The FWHM here is measured as 2.25 ±.02 ns. If we assume that the cosmic

ray coincidences give a delta function stimulation, then the FWHM of Fig. 20 is the system resolution time. The LED light pulse duration can then be estimated as,

$$t_{led} = \sqrt{(3.2)^2 - (2.25)^2} \text{ ns}$$
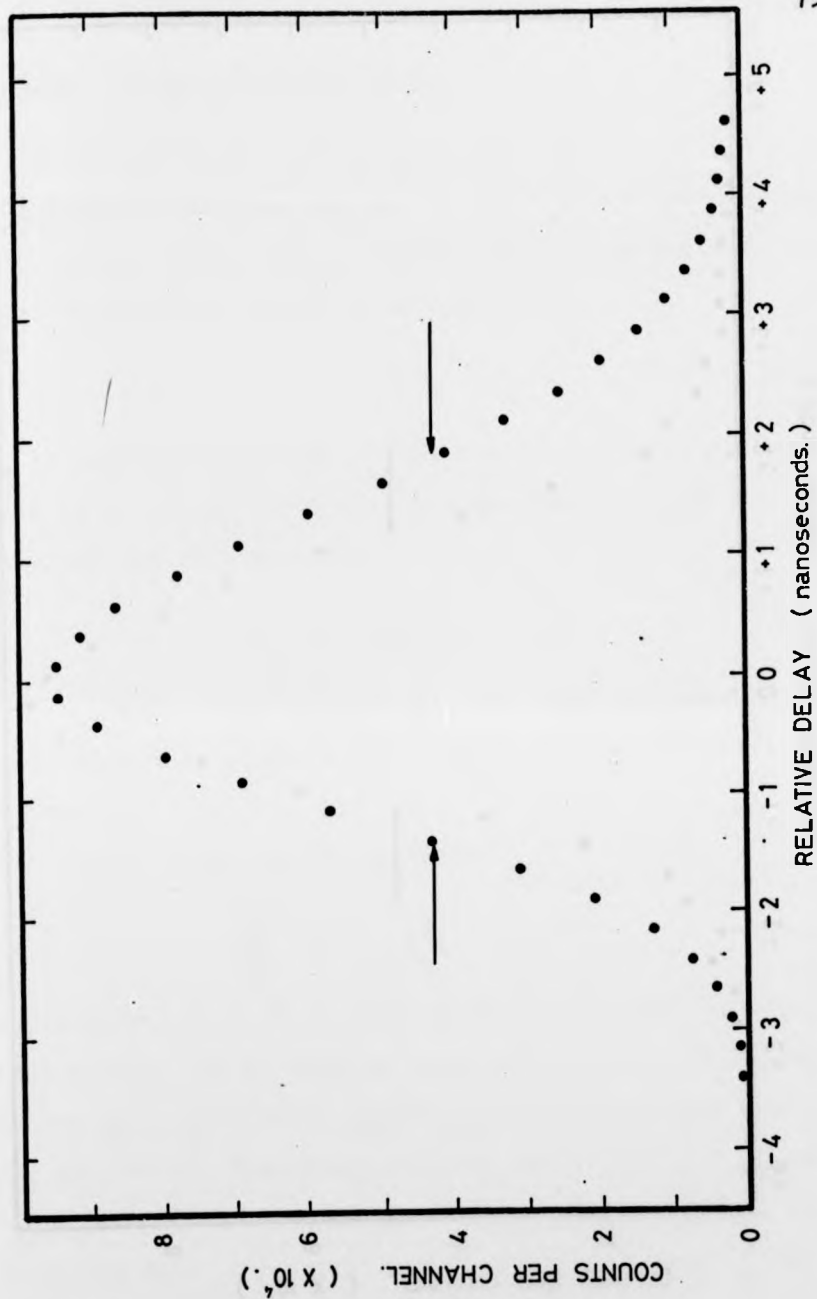
$$= 2.3 \text{ ns approximately.}$$

Fig. 19.

Coincidence peak produced by LED light pulser.

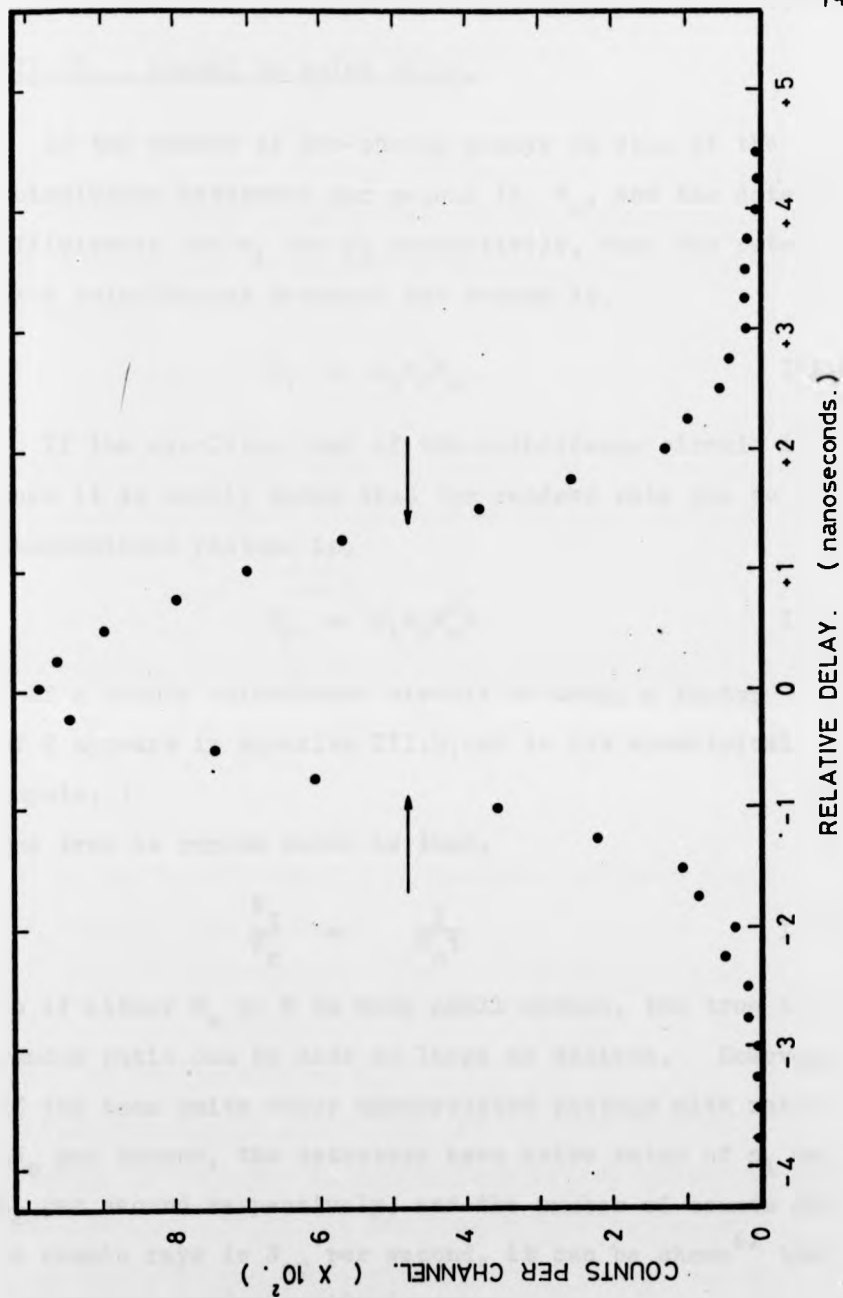Full width at half maximum = 3.2 ns.

Fig. 20.

Coincidence peak produced by cosmic rays.

Full width at half maximum = 2.25 ± .02 ns.

III.13. Signal to noise ratio.

If the number of two-photon decays in view of the coincidence detectors per second is N_o, and the detector efficiences are e_1 and e_2 respectively, then the rate of true coincidences detected per second is,

$$N_t = e_1 e_2 N_o \qquad \text{III.8.}$$

If the resolving time of the coincidence circuit is t, then it is easily shown that the randoms rate due to uncorrelated photons is,

$$N_r = e_1 e_2 N_o^2 t \qquad \text{III.9.}$$

(If a simple coincidence circuit is used, a factor of 2 appears in equation III.9, due to its symmetrical inputs.)

The true to random ratio is then,

$$\frac{N_t}{N_r} = \frac{1}{N_o t} \qquad \text{III.10.}$$

so if either N_o or t is made small enough, the true to random ratio can be made as large as desired. However, if the beam emits other uncorrelated photons with rate, aN_o per second, the detectors have noise rates of n_1 and n_2 per second respectively, and the number of counts due to cosmic rays is N_{cr} per second, it can be shown[62] that the true to randoms ratio is now,

$$\frac{N_t}{N_r} = \left[N_o t \left\{ 1 + \frac{n_1 + N_{cr}}{e_1 N_o} + a \right\} \left\{ 1 + \frac{n_2 + N_{cr}}{e_2 N_o} + a \right\} \right]^{-1} \qquad \text{III.11.}$$

Equation III.11 has a maximum value at,

$$N_o = (1 + a)^{-1} \left[\frac{(n_1 + N_{cr})(n_2 + N_{cr})}{e_1 e_2} \right]^{\frac{1}{2}} \qquad \text{III.12.}$$

Now the error in the number of true coincidences, in the presence of the random background, is, from Poisson statistics,

$$\Delta(N_t T) = \sqrt{N_t T + N_r T} \, ,$$

where T is the time taken to accumulate the time spectrum. The fractional error in the number of true counts is then,

$$f = \frac{\sqrt{(N_t + N_r)T}}{N_t T} \qquad \text{III.13.}$$

Substituting equation III.11 into equation III.13,

$$f = (e_1 e_2 T)^{-\frac{1}{2}} \left[\frac{1}{N_o} + t \left\{ 1 + \frac{n_1 + N_{cr}}{e_1 N_o} + a \right\} \left\{ 1 + \frac{n_2 + N_{cr}}{e_2 N_o} + a \right\} \right]^{\frac{1}{2}}$$
$$- \text{III.14.}$$

Now if the beam intensity is increased without limit, ($N_o \rightarrow \infty$), then we have,

$$f = (1 + a) \left[\frac{t}{e_1 e_2 \, T} \right]^{\frac{1}{2}} \qquad \text{III.15.}$$

which is independent on N_o.

Equation III.14 shows that the best statistical accuracy is achieved at the highest source strength, and from equation III.11, at the lowest true to random ratio.

In practice the onset of saturation limits the maximum count rates that can be tolerated. It can be seen, also, from Fig. 12, that N_o, which is proportional to the metastable density, and aN_o which is proportional to the neutral current, do not have a linear relationship as was

assumed above by introducing the factor a, certainly above about 1.1 keV,. Nevertheless, it can be seen that the region of maximum metastable density, around 1 keV, from Fig. 12, will give the best statistical accuracy, and therefore the best signal to noise ratio.

The expected background rate can be estimated from the number of photons emitted per second through collisional quenching of the metastables, R estimated in section II.4.3, page 32a. Since the metastable fraction of the total neutral beam has been estimated in section III.9, page 61, as about 0.1, and if we take as an upper limit, the same cross-section for emission of a photon by a ground state neutral in collision with a background gas molecule,as for a metastable atom, then the number of photons emitted per second by the total neutral beam is,

$$R' \cong 2.5 \ 10^5 \ s^{-1} \ .$$

The random coincidence rate produced by this background can be written, using equation III.9, as,

$$N_r = e_1 e_2 (R')^2 t$$

where e_1 and e_2 are the products of the quantum efficiencies and solid angles subtended at the beam by the two coincidence detectors respectively. We have, $e_1 e_2 \cong 2.8 \ 10^4$. t is the time delay per channel of the coincidence circuit, which is $2.5 \ 10^{-10}$ s. These values give,

$$N_r \cong 4.5 \ 10^{-3} \ s^{-1}$$

as the random background per coincidence channel.

IV.   Results and discussion.

IV.1.   Measurement method and data collection.

With a stable, dense metastable beam, produced by
1 keV protons at the optimum cesium thickness, the data
collection and measurement methods are as described below.

The oxygen flow to the metastable monitor Lyman-alpha
filter is increased until the count rate reaches an
equilibrium value.   Voltages of $\pm$ 250 V, and $\pm$ 45 V
are applied to the switch unit and the start button is
pressed.   The high and low voltages are switched
alternately to the pre-quench/proton removal plates,
which switch the metastable component of the beam off
and on respectively, through Stark quenching.

The output of the time to pulse height converter is
switched synchronously to subgroups A and B of the
multi-channel analyser memory.   The subgroups contain
200 channels each, and each channel represents a time
delay of $2.5 \ 10^{-10}$ s.

The monitored parameters are, apart from the coincidence
time spectra; the integrated singles counts, one of the
singles count rates, the metastable monitor output with
the metastable beam on and off, the metastable monitor
rate, the neutral detector current, and the integrated
beam on and beam off times.   The multi-channel analyser
also provides, as well as the time spectra directly, the
difference time spectrum, the integrated number of counts

in each of the three spectra, as well as the integral
under each peak.   The difference time spectrum s_hould
contain the two-photon peak. All these data are punched
on paper tape for later analysis, either by hand or by
computer, at the end of a run.

IV. 2.   Background radiation.

The singles rate,and therefore the randoms background,
was found to be critically dependent on slight changes
in the focussing conditions, and in the direction of the
beam, which tended to drift randomly with time.   As a
consequence, the signal to noise ratio could vary by up
a factor of two between different runs, which lasted
typically 20 hours.

The pressure dependence of the background was found to
be negligible, i.e., at about 3 10^{-8} torr in the detection
region,   a six-fold increase in pressure produced only
a 1% increase in the singles rate. It can be concluded,
then that the major contribution to the randoms background
is due to beam-surface collisions, either in the quartz
tube, or in chamber UHV II.   As a result, the normal
operating pressure in the detection region was allowed to
remain in the 10^{-8} torr range, the liquid nitrogen cold
traps being unfilled.

An optical spectrometer, observing (through a scectrosil
window) the proton beam striking a stainless-steel
surface, saw only the Balmer series of lines.   It can be
concluded that the Balmer-beta line is the main component
of the background radiation, since the photomultipliers

sensitivities are very low at the wavelength of the Balmer-alpha line, which is 486.1 nm.   The 9816QB photomultiplier tube always gave the highest singles count rate, when the beam was running, even though the quantum efficiencies of both photomultiplier tubes were similar, for since its spectral sensitivity extends to about 750 nm, it is sensitive to the Balmer-alpha line, although its sensitivity is much reduced at this wavelength.

Table IV.1 compares the number of random coincidences per memory channel observed, and those expected from the integrated singles counts.   The expected randoms count R per channel is calculated from equation III.9,

$$R \;=\; N_r T \;=\; \frac{N_1 N_2 t}{T} \qquad\qquad \text{IV.1.}$$

where N_1 and N_2 are the integrated singles counts from detectors 1 and 2 respectively, $(N_1 = e_1 N_o T \; ; \; N_2 = e_2 N_o T)$. The channel width, t, is fixed at $2.5 \; 10^{-10}$ s.   The more accurate formula for N_r, used in III.11 is not used as some of the parameters are not accurately known.   A small correction has to be applied owing to the different 'on' times of the singles circuit and the coincidence circuit.   The coincidence circuit is gated off for 0.655 s every minute, as mentioned in section III.11.2, and about a 1.5% correction is required.   The singles scalers also count the coincident signals, of course, but these are negligible compared with the randoms counts.

The agreement between the measured and calculated values is satisfactory, which indicates the correct operation of the circuits.

Run	T (sec.)	N_1 9816QB	N_2 XP1023	$R_{meas.}$	$R_{calc.}$	Ratio. (corr.)
50	$8.24\ 10^4$	$5.98\ 10^9$	$1.99\ 10^9$	$2.95\ 10^4$	$3.61\ 10^4$	0.83
52	$7.42\ 10^4$	$2.03\ 10^9$	$1.06\ 10^9$	$7.87\ 10^3$	$7.25\ 10^3$	1.09
53	$7.64\ 10^4$	$1.60\ 10^9$	$4.76\ 10^8$	$3.24\ 10^3$	$2.49\ 10^3$	1.31
54	$8.28\ 10^4$	$2.61\ 10^9$	$8.83\ 10^8$	$7.00\ 10^3$	$6.96\ 10^3$	1.01
55	$6.85\ 10^4$	$1.95\ 10^9$	$6.92\ 10^8$	$5.72\ 10^3$	$4.92\ 10^3$	1.17
56	$7.15\ 10^4$	$5.30\ 10^9$	$1.84\ 10^9$	$3.05\ 10^4$	$3.41\ 10^4$	0.90
60	$6.19\ 10^4$	$2.91\ 10^9$	$1.08\ 10^9$	$1.27\ 10^4$	$1.27\ 10^4$	1.01
61	$8.84\ 10^4$	$5.50\ 10^9$	$2.08\ 10^9$	$2.85\ 10^4$	$3.24\ 10^4$	0.89

Table IV.1.

Comparison of measured and calculated random coincidences per channel. T = Total time, N_1 = integrated singles count from photomultiplier 9816QB, N_2 = from XP1023, R_{meas} = measured number of random counts per channel, R_{calc} = number of random counts calculated. (see text) Ratio = R_{calc}/R_{meas} (corrected).

IV.3. The coincidence peak.

The spurious coincidences, presumably due to cosmic rays, arrive at a constant rate, depending only on the geometry and sensitivity of the detection system, and independently of all other conditions in the apparatus. This rate is about 0.25 s^{-1}, and gives rise to relatively large peaks in the coincidence spectra for the metastable beam on and and for the metastable beam quenched. On subtracting these spectra the residual coincidence peak is observed, approximately half the size of the spurious peak, under the optimum conditions expected for observation of the two-photon decay.

The number of counts under the peak is observed to be proportional to the metastable density, for a constant detection geometry. These coincidences are ascribed to the two-photon decay of metastable atomic hydrogen, and a number of tests will be described below which confirm this belief.

Difference time spectra obtained by the method described in section 1 are shown in Fig. 21 and Fig. 22. The total times taken to obtain these spectra were about 21 hours each. The number of counts under the peaks is about 4,000 in each case. Each point shown in the figures is the sum of two adjacent multi-channel analyser memory channels. The time delay corresponding to each point is then 0.5 ns. Both curves display a full width at half maximum of about 4.5 points as shown, or 9 memory channels, which gives the FWHM of each curve as about 2.25 ns.
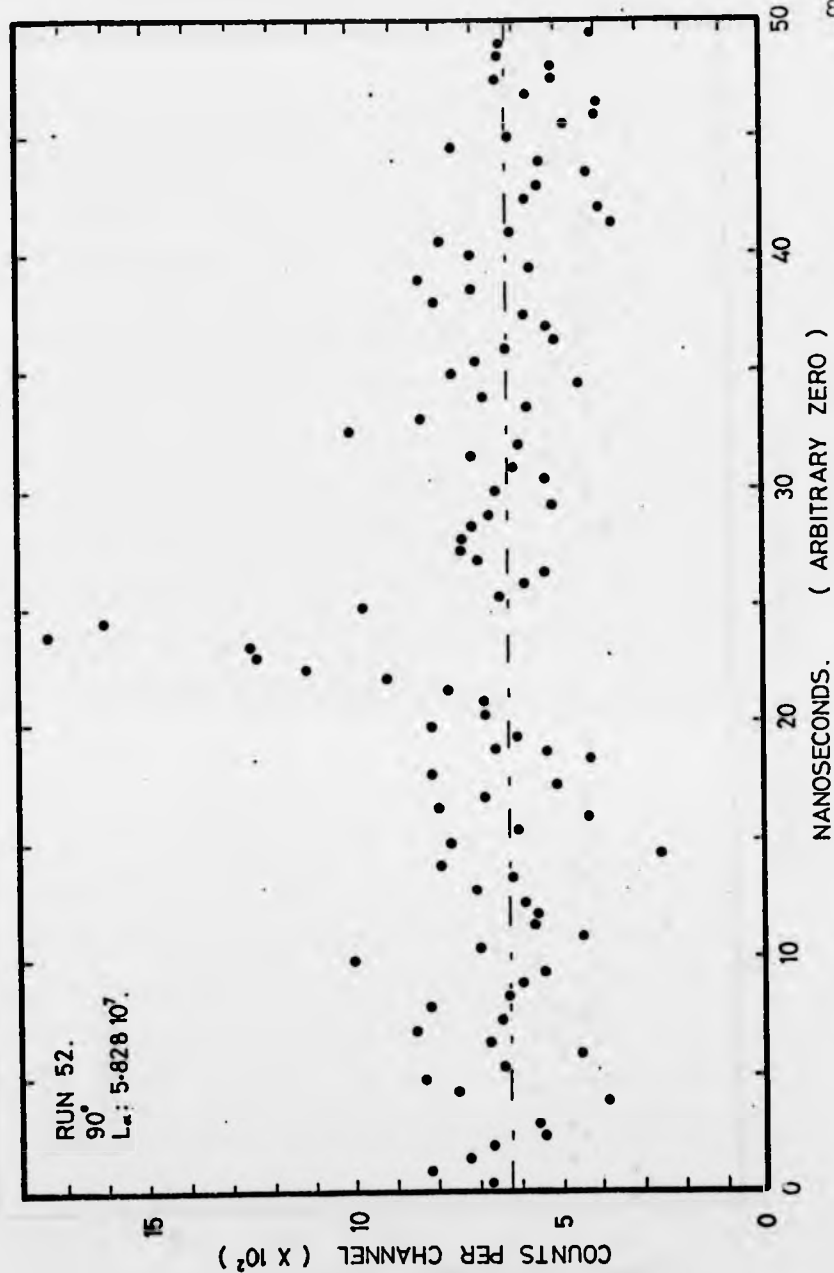
RUN 52.
90°
L₀: 5·828 ×10⁷.

Fig. 21.

Coincidence curve with a metastable beam passing
through detection region, angle between detectors
90°. Each point represents delay of 0.5 ns.
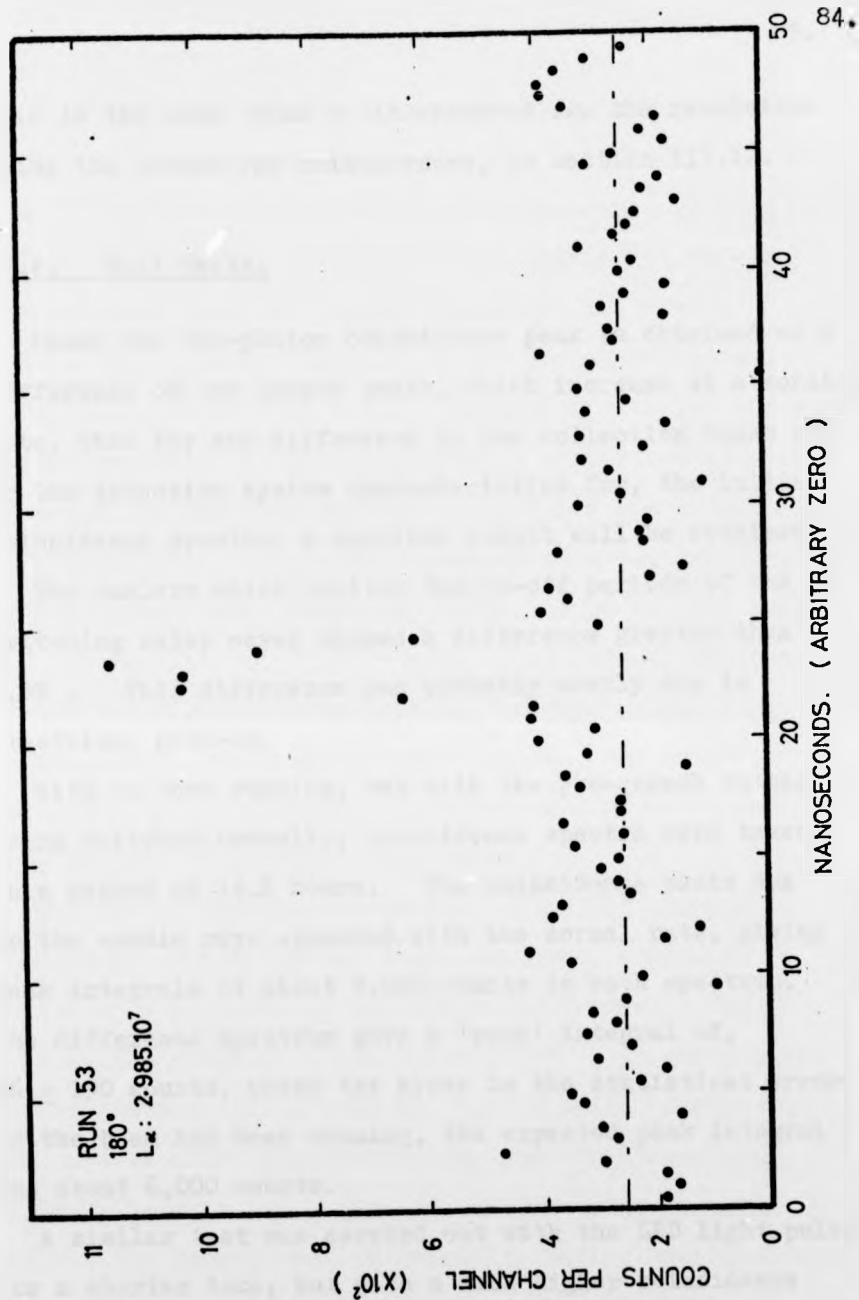Total time about 21 hours.

Fig. 22.

Same as fig. 21, but with angle between detectors
at 180°.   Total time about 21 hours.

This is the same value as is observed for the resolution using the cosmic ray coincidences, in section III.12.

IV.4.   Null tests.

Since the two-photon coincidence peak is obtained as a difference of two larger peaks, which increase at a constant rate, then for any difference in the collection times of, or the detection system characteristics for, the initial coincidence spectra, a spurious result will be obtained.

The scalers which monitor the on-off periods of the switching relay never showed a difference greater than 0.3% .   This difference was probably mostly due to electrical pick-up.

With no beam running, but with the pre-quench voltage being switched normally, coincidence spectra were taken in a period of 14.2 hours.   The coincidence peaks due to the cosmic rays appeared with the normal rate, giving peak integrals of about 9,000 counts in each spectrum. The difference spectrum gave a 'peak' integral of, 46 $\pm$ 190 counts, where the error is the statistical error. If the beam had been running, the expected peak integral was about 6,000 counts.

A similar test was carried out with the LED light pulser, for a shorter time, but with a much higher coincidence rate.   The result was again zero within the error .

A null test, identical to the first one described above, but with a hot-wire ionization gauge switched on in one of the vacuum chambers to simulate the background due to the beam, was run for a period of about 37 hours.

In this case the singles rates were about 20% of their
normal values with the beam running.   Again a null result
was obtained, with a difference peak integral of 84 ± 300.

Fig. 23 shows the coincidence spectrum obtained when
a metastable beam was running normally, but with a
voltage of ± 1,000 V applied to the pre-quench wires,
(position (9) in Fig. 5.).   The voltage to the pre-quench
plates was being switched as usual.   The expected number
of counts in the peak was about 8,200, or a peak height
of about 2,500.   This was estimated from the metastable
monitor count rate immediatly before and after the run,
and the neutral detector output, which gave an indication
of the beam stability throughout the run.   The
actual number of counts measured at the peak location
was 240 ± 900.   A number of such runs were made, and
each one was null within the error.

The count distribution in Fig. 23 is not symmetrical
about zero, which implies that some other component of
the beam is affected by the switching system.   This
must be the residual charged component.   It was pointed
out in section III.7, page 53, that a small fraction of
the protons enter the quartz tube when the pre-quench
plate voltage is low.   The pre-quench wires do not
deflect the proton beam efficiently, having been designed
to perform the opposite function.   This test then shows
that the residual charged component of the beam does not
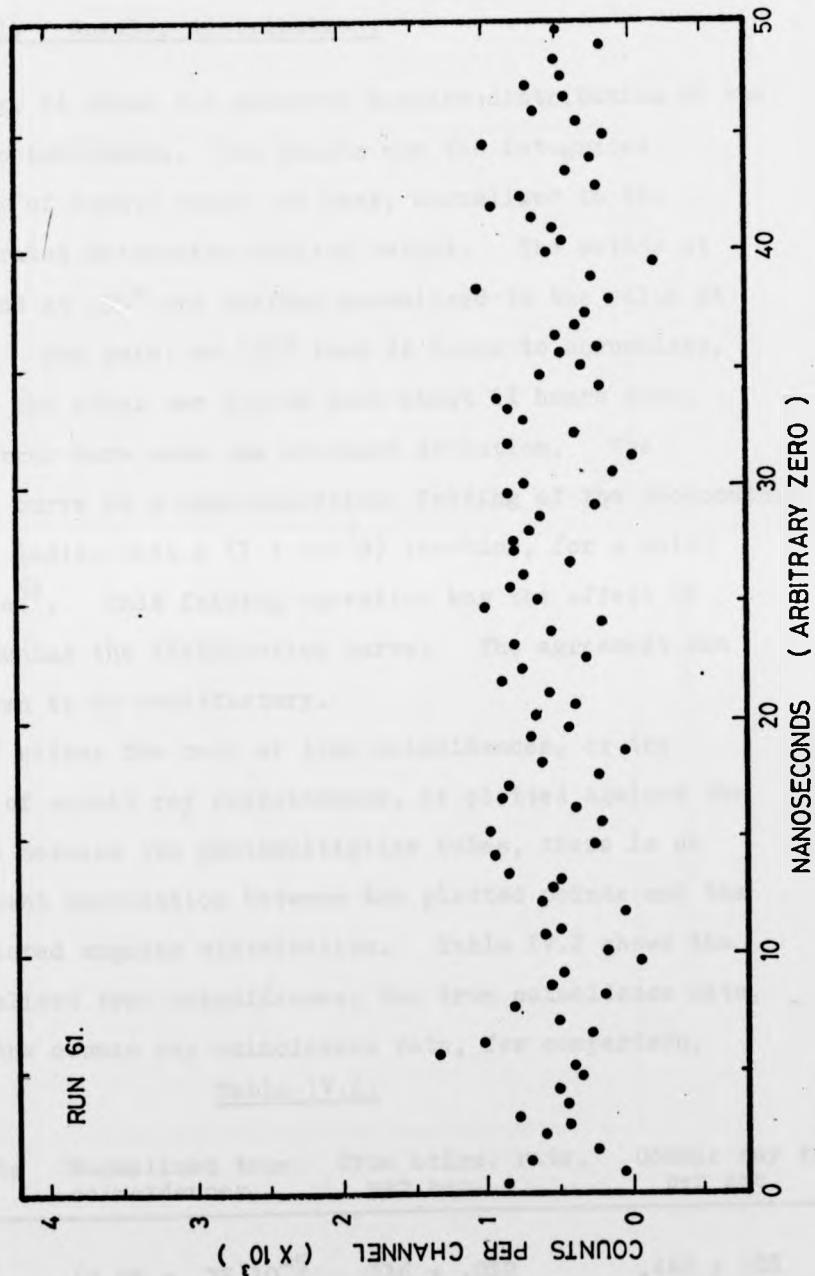produce coincidences.

RUN 61.

COUNTS PER CHANNEL (X 10³)

NANOSECONDS (ARBITRARY ZERO)

Fig. 23.

Coincidence spectrum with metastables fully quenched.

Total time about 22 hours.

IV.5.   Observed characteristics of the two-photon decay.

IV.5.1.   Angular distribution.

Fig. 24 shows the measured angular distribution of the
true coincidences. The points are the integrated
number of counts under the peak, normalised to the
integrated metastable monitor output.   The points at
90° and at 135° are further normalised to the value at
180°.   The point at 135° took 42 hours to accumulate,
while the other two points took about 21 hours each.
The error bars show one standard deviation.   The
solid curve is a semi-analytical folding of the photocathode
solid angles with a $(1 + \cos^2\theta)$ function, for a point
source.[63].   This folding operation has the effect of
flattening the distribution curve.   The agreement can
be seen to be satisfactory.

If either the rate of true coincidences, or the
rate of cosmic ray coincidences, is plotted against the
angle between the photomultiplier tubes, there is no
apparent correlation between the plotted points and the
predicted angular distribution.   Table IV.2 shows the
normalised true coincidences, the true coincidence rate,
and the cosmic ray coincidence rate, for comparison.

Table IV.2.

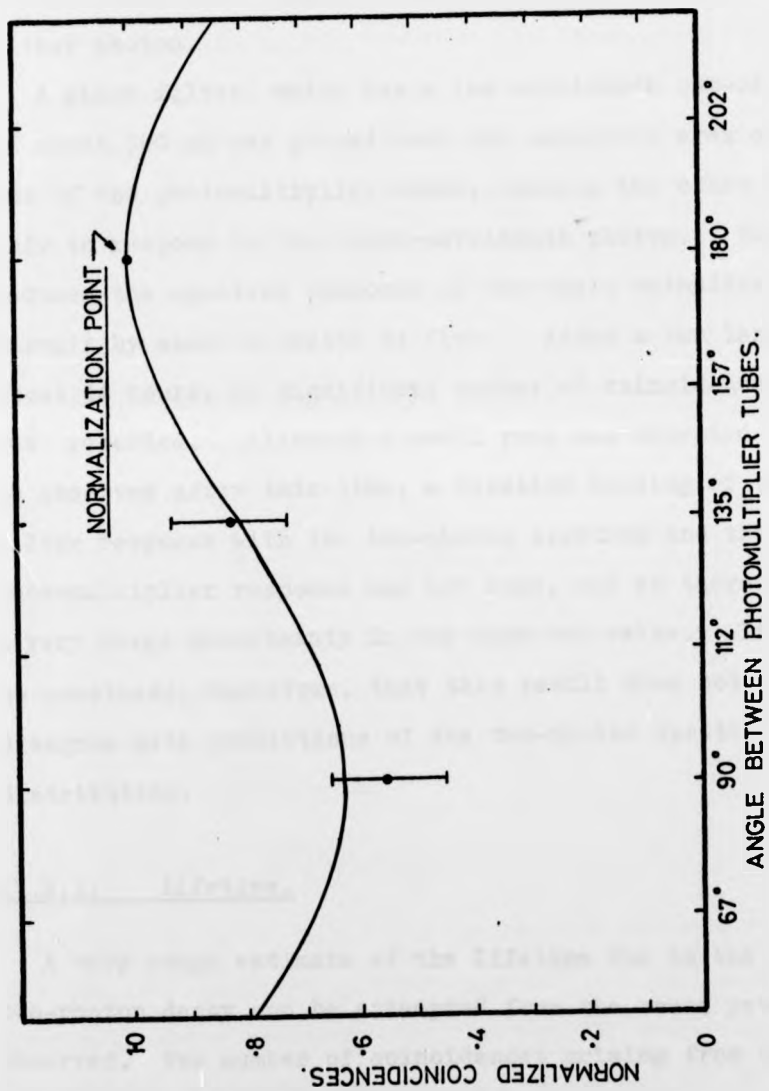| Angle	Normalised true coincidences.	True coinc. rate. per sec.	Cosmic ray rate. per sec.
90°	$(7.85 \pm .75)10^{-5}$	$.116 \pm .012$	$.442 \pm .01$
135°	$(1.18 \pm .10)10^{-4}$	$.114 \pm .014$	$.238 \pm .01$
180°	$(1.42 \pm .10)10^{-4}$	$.112 \pm .008$	$.289 \pm .01$

Fig. 24.

Normalised coincidence peaks at 180°, 135°, and 90°
compared with predicted angular distribution.

IV.5.2.   Spectral distribution.

The photomultiplier tubes respond to about 56% of the
two-photon spectrum, and since the spectral sensitivities
of both tubes are similar, either tube can respond to
either photon.

A glass filter, which has a low wavelength cut-off
of about 300 nm was placed over the sensitive area of
one of the photomultiplier tubes, causing the other tube
only to respond to the short-wavelength photon.   This
reduces the spectral response of the whole coincidence
circuit by about a factor of five.   After a run lasting
about 44 hours, no significant number of coincidences
was recorded.   Although a small peak was expected to
be observed after this time, a detailed folding of the
filter response with the two-photon spectrum and the
photomultiplier response was not done, and so there is
a very large uncertainty in the expected value.   It can
be concluded, therefore, that this result does not
disagree with predictions of the two-photon spectral
distribution.

IV.5.3.   Lifetime.

A very rough estimate of the lifetime due to the
two-photon decay can be attempted from the count rates
observed.   The number of coincidences arising from the
two-photon decay can be expressed as,

$$N(2\gamma) = \frac{j(2S)}{v} l\eta\, G\, FA \qquad\qquad IV.2.$$

where $j(2S)$ is the flux of metastables through the quartz
tube; v is the beam velocity, about $4.4\ 10^7$ cm s^{-1};
G is the geometrical factor for coincidence detection,
including the $(1 + \cos^2\theta)$ term, which has been calculated[63]
to be, $1.5\ 10^{-2}$; l is the length of the observation,
about 3 cm; η is the product of the peak quantum
efficiencies of the coincidence photomultipliers, about $7\ 10^{-2}$;
F is the fraction of the two-photon spectrum which can be
observed, about 0.56 ; A is the transition probability
for the two-photon decay.

The metastable flux can be found from the metastable
monitor output, which can be expressed as,

$$N(L_\alpha) = j(2S)\cdot g \qquad\qquad IV.3.$$

where g is the overall efficiency of the metastable monitor,
which is, from section III.9, $8.1\ 10^{-8}$.

Eliminating $j(2S)$ from IV.2 and IV.3, we get the
transition probability as,

$$A = \frac{N(2\gamma)}{N(L_\alpha)}\frac{gv}{\eta\, G\, lF} \qquad\qquad IV.4.$$

The quantity $N(2\gamma)/N(L_\alpha)$ can be taken from table IV.4.2,
for the 180° position as about $1.4\ 10^{-4}$. (The geometrical
factor G above is calculated for the 180° position.)
Substituting all these values in IV.4 we get for the
transition probability,

$$A = 0.6\ s^{-1} \quad \text{or} \quad t_{2S} = 1.7\ s$$

The predicted lifetime is[9], 0.12153 ± .00002 s.
Considering the very large uncertainties in the above
estimate, which are difficult to estimate themselves, but
are expected to be at least a factor of 10, the measured
value of 1.7 s can not be considered to be in disagreement
with the theoretical prediction.

IV.6.   Suggestions for future work.

The apparatus is capable of running continuously for
100 hours or more with the minimum of attention.   It
should thus be possible to reduce the size of the error
bars on the points for the angular distribution curve, and
observe at a much greater number of angles.

A solar-blind photomultiplier tube is available, with
spectral sensitivity extending from 120 nm to 300nm, but
with a small sensitive area and   low quantum efficiency,
and gain.   However, it is not sensitive to the Balmer
series and thus substantially reduces the random background.
Because of its smaller size, the expected angular distribution
curve should be less flattened, and so a much more
accurate measurement of this quantity should be obtained.

The spectral distribution could be determined using
broadband filters and very long measuring times.

The metastable monitor could be calibrated absolutely
and the coincidence photomultipliers calibrated as well,
and the geometry of the detecting systems determined more
accurately, to give the first direct measurement of the
metastable hydrogen lifetime, probably with an error of
about 50%.

IV.7.   Conclusion.

On the basis of the tests and measurements described
above, it can be concluded that the coincidences observed
are associated with the $2S_{\frac{1}{2}}$ state of atomic hydrogen.
The observation of the angular dependence of the coincidences
make unlikely the possibility that they arise from cascades,
excited in some way by the metastable state.   Cascades
would also be expected to produce an observable 'tail' in
the shape of the coincidence curve.   It can be finally
be concluded that the two-photon decay of metastable
atomic hydrogen has been observed, and its measured
characteristics are in agreement with predictions.

References.

1. Bohr,N., Phil.Mag., 26, 1, (1913).

2. Series,G.W. Spectrum of Atomic Hydrogen, Oxford
   University Press, London, 1957.

3. Lamb,W.E., and Retherford,R.C., Phys.Rev., 79, 549,
   (1950).

4. Bethe,H.A., Phys.Rev., 72, 339, (1947).

5. Akhiezer,A.I., and Berestetskii,V.B., Quantum
   Electrodynamics, Interscience, New York, (1965)

6. Breit,G., and Teller,E., Astrophys.J., 91, 215, (1940).

7. Goppert-Mayer,M., Ann.Phys., 9, 273, (1931).

8. Shapiro,J., and Breit,G., Phys.Rev., 113, 179, (1959).

9. Klarsfeld,S., Phys.Lett., 30A, 382, (1969).

10. Salpeter,E.E., Phys.Rev., 112, 1642, (1958).

11. Feinberg,G., Phys.Rev., 112, 1637, (1958).

12. Zel'dovich,Ya.B., and Perelemov,A.M., JETP, 12, 777,
    (1961).

13. Eichter,T., et al., Phys.Lett., B46, 281, (1973).

14. Marrus,R., and Schmieder,R.W., Phys.Rev.A, 5,1160, (1972).

15. Garstang,R.H., Publ.Astron.Soc.Pac., 81, 488, (1969).

16. Fite,W.L., Brackmann,R.T., Hummer,D.G., and
    Stebbings,R.F., Phys.Rev., 116, 363, (1959).

17. Spitzer,Jr.,L., and Greenstein,J.L., Astrophys.J.,
    114, 407, (1951).

18. Lipeles,M., Novick,R., and Tolk,N., Phys.Rev.Lett.,
    15, 690, (1965).

19. Artura,C.J., Tolk,N., and Nocick,R., Astrophys.J.,
    157, L181, (1969).

20. Kocher,C.A., Clendenin,J.E., and Novick,R.,
    Phys. Rev. Lett., 29, 615, (1972).

21. Schmieder,R.W., and Marrus,R., Phys. Rev. Lett.,
    25, 1612, (1970).

23. Prior,M.H., and Shugart,H.A., Phys. Rev. Lett.,
    27, 902, (1971).

24. Prior,M.H., Phys. Rev. Lett., 29, 611, (1972).

25. Van Dyck,Jr.,R.S., Johnson,C.E., and Shugart,H.A.,
    Phys. Rev. Lett., 25, 1403, (1970).

26. Pearl,A.S., Phys. Rev. Lett., 24, 703, (1970).

27. Moos,H.W.,and Woodworth,J.R.,Phys. Rev. Lett., 29, 615,
    (1973).

28. Bräunlich,P., Hall,R., and Lambropoulos,P,
    Phys. Rev. A, 5, 1013, 1013, (1972).

29. Zernik,W., Phys. Rev. 132, 320, (1963); 133, A118, (1964).

30. Öed,P., private communication.

31. Kleinpoppen,H., private communication.

32. Donnally,B.L., Clapp,T., Sawyer,W., and Schultz,M.,
    Phys. Rev. Lett., 12, 502, (1974).

33. Sellin,I.A., and Granoff,L., Phys. Lett., 25A, 484, (1967).

34. Spiess,G., Valance,A., and Pradel,P., Phys. Rev. A,
    6, 746, (1972).

35. Pradel,P., Roussel,F., Schlachter,A.S., Spiess,G.,
    Phys. Rev. A, 10, 797, (1974).

36. Marcuse,D., Eingineering Quantum Electrodynamics.
    Harcourt, Brace, & World, Inc., New York, (1970).

37. Bethe,H., and Salpeter,E.E., Quantum Mechanics of
    One-and Two-Electron Atoms. Springer-Verlag,
    Berlin, (1957).

38. Shapiro,J., and Breit,G., Phys. Rev. 113, 179,(1959).

39. Drake,G.W.F., and Grimley,R.B., Phys. Rev. A, 8, 157, (1973).

40. Dose,V., and Guńz,R., J. Phys. B, 5, 1412, (1972).

40a. Dose,V., and Gunz,R,, J.Phys. B., 5, 636, (1972).

41. Dose,V., Meyer,V., and Salzmann,M., J. Phys. B, 2, 1357, (1969).

42. Byron,F.W., Krotkov,R.V., and Medeiros,J.A., Phys. Rev. Lett., 24, 83, (1970).

43. Bell,R.E.Alpha, Beta, and Gamma-ray Spectroscopy, Edited by K. Siegbahn, North Holland Amsterdam, (1968).

44. Kauppila,W.E., Ott,W.R., and Fite,W.L., Phys. Rev. A, 1, 1099, (1970).

45. Bayfield,J.E., Phys. Rev., 182, 115, (1969).

49. Cleaver,J.S., and Fiveash,P.N., Vacuum, 20, 49, (1970).

50. Bacal,M., Truc,A., Doucet,H.J., Lamain,H., and Chretien,M., Nucl. Instr. Meth., 114, 407, (1974).
     Bacal,M., and Reichelt,W., Rev. Sci. Instr., 20, 769, (1974).

52. Taylor,J., and Langmuir,I., Phys. Rev. 51, 753, (1937).

55. Sellin,I.A., Phys. Rev., 136, A1245, (1964).

56. Tuan, Vu Ngoc, Gautherin,G., Schlachter,A.S., Phys. Rev.A, 9, 1242, (1974).

57. Carriere,J.D., and de Heer,F.J., J. Chem. Phys., 56, 2993, (1972).

58. van Wijngaarden,A., Drake,G.W.F., and Farago,P.S., Phys. Rev. Lett., 33, 4, (1974).

59. Novick,R., Physcics of the One- and Two-electron Atoms, Edited by Bopp,F., and Kleinpoppen,H., North Holland, Amsterdam, (1969).

60. King,G.C., Read,F.H., and Imhof,R.E., J. Phys. B,
                                    (to be published).

61. The Use of Transistors in Avalanche Mode, Ferranti Ltd.,
                      .   Application note.

62. Imhof,R.E., Ph.D. thesis, Manchester University,
                                    1972, (unpublished).

63. Duncan,A.J., private communication.

*47. Massey,H.S.W., Rept Prog. Phys., 12, 248, (1949).

ERRATA.

Page 10, line 5, should begin:

"of singly-stimulated two-photon emission ... ".

Page 12, equation II.1., and subsequent equations, replace "h" by "$\hbar$".

Page 15, equation II.10., replace "A" by "$\vec{A}$".

Page 15, equation II.12., and page 19, equation II.23., insert modulus brackets around the respective matrix elements before squaring.

Page 19, last line should read: "Substituting equation II.24. in equation II.23,".

Page 26, equation II.36., the multiplying factor should be: $\omega_2^3 \omega_1^3 d\omega_1$.

Page 39, line 8, delete "which".

Page 69, line 4, read "gated" for "geted".

Page 70, line 4, read "limited" for "limeted".

Page 93, reference 13 should read:

"Hasert,F.J., et. al., Phys. Lett., 46B,138, 1973.